Ocean Modelling 203 (2026) 102780

Contents lists available at ScienceDirect

Ocean Modelling

journal homepage: www.elsevier.com/locate/ocemod

Sensitivity of simulated storm surge to tropical cyclone wind forcing around islands: insights from Hurricane Irma

A. Zribi [a,b,*], S. Jullien [a], N. Herry [c], X. Bertin [b], G. Dodet [a]

[a] Univ Brest, CNRS, Ifremer, IRD, Laboratoire d'Océanographie Physique et Spatiale (LOPS), IUEM, F-29280, Plouzané, France
[b] UMR7266 LIENSs, CNRS - La Rochelle University, 2 rue Olympe de Gouges, La Rochelle, 17000, France
[c] Institut de Recherche pour le Développement, UMR 250 ENTROPIE (IRD, CNRS, Ifremer, Université de la Réunion, Université de la Nouvelle-Calédonie), BP A5, 98848, Nouméa, New Caledonia

ARTICLE INFO

Dataset link: https://data.shom.fr, https://www.ioc-sealevelmonitoring.org/station.php?code=barb, https://www.ncei.noaa.gov/products/international-best-track-archive, https://cyclobs.ifremer.fr/app/tropical, https://doi.org/10.12770/11057ae4-b708-481a-9848-2e4fdef57625, https://cds.climate.copernicus.eu/datasets/reanalysis-era5-single-levels?tab=overview, https://data.marine.copernicus.eu/product/GLOBAL_MULTIYEAR_PHY_001_030/description, https://doi.org/10.5281/zenodo.15064113

Keywords:
Storm surge
Tropical cyclone
Uncertainties
Parametric forcing
Modelling
Hurricane Irma

ABSTRACT

In September 2017, Category-5 Hurricane Irma made landfall on the small islands of Barbuda and Saint Martin, causing exceptional and devastating storm surges. Understanding such extreme surges is essential for improving their forecast and designing effective risk management strategies. One of the main challenge for their accurate modelling lies in the strong uncertainties in the characterisation and representation of tropical cyclone (TC) atmospheric conditions. The present study investigates the sensitivity of simulated surge to TC position, wind intensity, structure, and surface stress formulation, through experiments based on scenarios exploring their range of uncertainty. Simulations with the Coastal and Regional Ocean COmmunity model reveal that the surge peak (over 2 m) at two tide gauge locations is primarily driven by extreme winds in the cyclone eyewall, and is correctly captured only when specific cyclone track and wind stress intensity are met, while being completely missed when relying on global atmospheric reanalysis winds. Relative to a reference simulation, changes in the wind stress formulation or the TC position reveal variations in the peak surge amplitude of up to 52% and 44%, respectively. Meanwhile, the peak surge duration is highly sensitive to the wind structure. The impact of structure and track is also shown to be strongly site-dependent. These results highlight the need for realistic cyclone intensities, structures, and tracks for an accurate surge modelling, especially when intense cyclones pass over, or at a few kilometres, from volcanic islands. They also provide guidance on the TC uncertainties to be accounted for when simulating surge, since deriving cyclone characteristics, even from state-of-the-art observations, remains challenging.

1. Introduction

Storm surges induced by tropical cyclones (TCs) are among the most deadly and damaging natural disasters (Needham et al., 2015). Between 1850 and 2000, they were responsible for 10,000 to 15,000 deaths each year (Nicholls, 2006). Individual events can have catastrophic impacts, such as cyclone Nargis, which caused nearly 140,000 deaths in Myanmar in 2008 (OCHA, 2008), even though the frequency of such high-fatality events is declining in most regions worldwide, reflecting improvement in risk reduction efforts (Bouwer and Jonkman, 2018). Meanwhile, the concentration of population and economic activities in coastal areas keep increasing: in 2020, nearly 11% of the global population, around 896 million people, live in coastal areas that do not exceed 10-m elevation above mean sea level (Haasnoot et al., 2021), and this number is projected to exceed one billion by 2050 (Oppenheimer et al., 2019). In next decades, coastal risks are expected to further intensify under climate change and sea-level rise (Neumann et al., 2015; Muis et al., 2016; Glavovic et al., 2022).

Storm surges are positive sea-level anomalies primarily driven by wind stress and atmospheric pressure gradients, in combination with astronomical tides. They can include non-linear tide-surge interactions (Proudman, 1957), and significant short-waves contributions (Lavaud et al., 2020). Nowadays, numerical models represent essential tools for predicting storm surges at the coast, investigating the inherent physical processes, and providing valuable information for adaptation strategies. A key requirement for reliable simulations is the accurate representation of TC atmospheric forcing. In particular, previous studies have shown that storm surge simulations are strongly influenced by TC wind intensity (Rego and Li, 2009; Weisberg and Zheng, 2006), intensification rate in rapidly intensifying systems (Sebastian and Behera, 2022), storm size as characterised by the radius of maximum winds (Irish et al., 2008; Kang et al., 2026), and forward speed (Peng

* Corresponding author.
E-mail address: aline.zribi@ifremer.fr (A. Zribi).

https://doi.org/10.1016/j.ocemod.2026.102780
Received 27 December 2025; Received in revised form 25 April 2026; Accepted 8 June 2026
Available online 15 June 2026

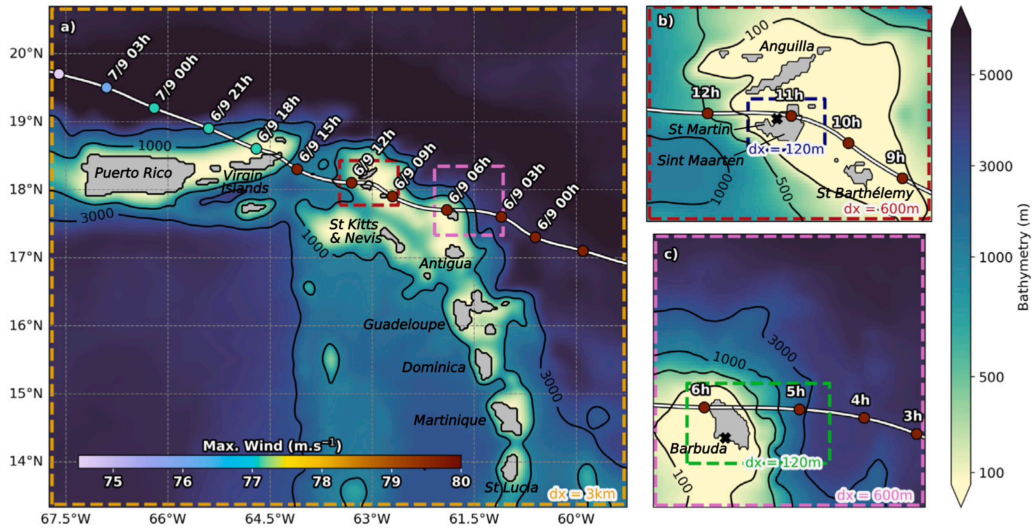

Fig. 1. Ocean model configurations showing the parent domain (a), along with the two nests for Saint Martin (b) and Barbuda (c). Domain boundaries are shown as dashed lines, bathymetry is displayed in colour shading, the cyclone track is indicated in white with dots coloured by IBTrACS wind intensity, and black crosses in (b) and (c) mark the locations of the tide gauges. Several modelled iso-depth are indicated with black lines, labelled in metres.

et al., 2006; Rego and Li, 2009; Thomas et al., 2019). Additional sensitivities arise from landfall angle (Weisberg and Zheng, 2006; Ramos-Valle et al., 2020) and timing relative to the tidal phase (Thomas et al., 2019), leading to highly location-dependent impacts. Uncertainties also persist in the parametrisation of surface stress, a key driver of surge generation (e.g. Moon et al., 2009; Bertin et al., 2015; Pineau-Guillou, 2018), with no clear consensus yet established (Bryant et al., 2016). Despite significant progress in observing and understanding TC dynamics over recent decades (Emanuel, 2018), including the emergence of high-resolution satellite measurements such as Synthetic Aperture Radar (SAR, e.g. Mouche et al., 2017, 2019), in situ and remote observations remain sparse. As a result, the characterisation of TC atmospheric conditions is still subject to substantial uncertainty, even in post-event best-track datasets (Torn and Snyder, 2012; Landsea and Franklin, 2013). In this context, this study aims to assess how these uncertainties in TC forcing translate into variations in simulated storm surges. We conduct a set of surge simulations using the Coastal and Regional Ocean COmmunity (CROCO) ocean model, forced with state-of-the-art parametric TC wind field. Each experiment explores the impact of variations in key TC characteristics, namely wind stress formulation, storm structure, and track parameters, within their respective observational uncertainty ranges. These ranges are derived from the known limitations in post-event and real-time TC observations, and are used here to define physically plausible scenarios. The analysis of this set of deterministic sensitivity experiments contributes to improve the understanding and modelling of TC-induced storm surges, which is essential for better characterising this hazard and developing more effective coastal adaptation strategies.

In September 2017, TC Irma developed offshore Cape Verde islands, and travelled across the Atlantic towards the Caribbean Arc (Fig. 1). Irma caused 47 direct fatalities, and significant storm surges, particularly across the northern Caribbean arc and Florida (Cangialosi et al., 2021). It became one of the strongest and costliest TC ever recorded in the North Atlantic basin. As a Category-5 hurricane, Irma made landfall at Barbuda (Fig. 1) around 05:45 UTC, with maximum winds of 80 m.s^{-1} and a minimum pressure of 914 hPa. The hurricane caused 3 fatalities, and destroyed about 95% of the island's structures, rendered it nearly uninhabitable. A few hours later, around 11:15 UTC, Irma made a second landfall on Saint Martin island (Fig. 1) with the same intensity, causing 15 fatalities, and damaging 90% of buildings (Cangialosi et al., 2021). Some previous studies have already investigated the sensitivity of modelled storm surges associated with TC Irma to various aspects of the atmospheric forcing. So et al. (2019) modelled intense positive and negative storm surges (exceeding ± 2 m) along the wide continental shelf of the Florida peninsula, which were strongly linked to spatial gradients in wind stress. Surges in this region were also simulated in Dullaart et al. (2020), which highlighted the improved performance of global surge models due to advances in climate reanalysis products. Recently, Chaigneau et al. (2024) explored the sensitivity of storm surges in Florida and Puerto Rico to multiple factors, including the wind stress parametrisation and the choice of atmospheric forcing, through comparisons between different parametric wind models and a global reanalysis, the latter generally providing more accurate results. Interestingly, extreme surges were reported in Saint Martin and Barbuda (Rey et al., 2019; Arpaia et al., 2021; Cangialosi et al., 2021), although such high values are unusual for small tropical islands with narrow continental shelves as shown by Kennedy et al. (2012). The availability of tide gauge observations on both islands provides an opportunity to investigate how storm surge generation on these islands, located only a few kilometres from the track of a Category-5 cyclone, is sensitive to the TC wind forcing characterisation. Our results lead to distinct conclusions from those drawn in previous regional studies (Dullaart et al., 2020; Chaigneau et al., 2024) regarding the atmospheric forcing requirements for accurate surge modelling. These differences are attributed to the particular sensitivity of volcanic islands to extreme and sharply varying wind fields, and their uncertainties.

The paper is organised as follows. Section 2 describes the methodology, including the configuration of the CROCO ocean model, the atmospheric forcing used, and the design of the numerical experiments. The main results of the sensitivity experiments are presented in Section 3, and discussed in Section 4, along with the limitations arising from the parametric representation of TC winds and missing wave effects. Section 5 provides concluding remarks.

2. Materials and methods

2.1. TC best-track data

As a collaborative effort between all World Meteorological Organization (WMO) Regional Specialized Meteorological Centres (RSMCs), the International Best Track Archive for Climate Stewardship (IBTrACS; (Knapp et al., 2010; Gahtan et al., 2024), D0I v4r01: 10.25921/82ty-9e16) is the reference dataset for TC main characteristics.

It combines all available observations (storm reports, buoys, ships, radar, aircraft, satellites, etc.) to produce the best possible estimate of the TC track, intensity, and characteristic radii. From this dataset, the following parameters, as provided by the USA agency, are used to build the atmospheric forcing of TC Irma (as detailed in Section 2.3):

- the TC centre position (longitude and latitude)
- the 1-minute maximum sustained wind speed
- the characteristic radii at 34-, 50-, and 64-kt, in each quadrant (North-East, South-East, South-West and North-West). These radii represent the maximum radial extent at which the respective wind thresholds are reached in each quadrant.

Along with the best-track data, IBTrACS provides estimates of uncertainties in TC position and wind intensity. These uncertainties largely depend on the year of occurrence, the TC intensity, the ocean basin and the type of observations available. In particular, the availability of aircraft reconnaissance data (in the Western Pacific from 1950 to 1987 and in the North Atlantic since 1950) or the proximity to the U.S. coasts contribute to reduced uncertainty levels (Landsea and Franklin, 2013). Positional uncertainty in IBTrACS is derived from comparing the TC positions reported by different agencies. This uncertainty generally decreases with increasing wind intensity, as stronger TCs tend to exhibit a more clearly defined eye, making the centre position easier to identify. For Irma, winds exceed 51 m.s^{-1} (100 kt) when it passed over Barbuda and Saint Martin, the position uncertainty is then estimated to range between 10 and 15 km. Intensity uncertainty in IBTrACS is based on qualitative expert assessments. For Irma, a post–2000 North Atlantic TC, the estimated uncertainty is approximately $\pm$ 3.6 m.s^{-1} (7 kt). The impact of these uncertainties on the modelled storm surge will be assessed with several sensitivity tests described in Section 2.4.

2.2. The CROCO ocean model

Numerical simulations of the storm surges induced by Hurricane Irma are carried out with the Coastal and Regional Ocean COmmunity model, version 2.1.0 (CROCO; DOI: 10.5281/zenodo.15064113). CROCO is a free surface oceanic model running on a structured mesh with a split-explicit time-stepping scheme and terrain-following S-coordinates. In this study, the model is configured to solve the three-dimensional incompressible primitive equations under the hydrostatic and Boussinesq approximations. Seawater density is computed from a non-linear equation of state as a function of potential temperature, salinity and pressure (Shchepetkin and McWilliams, 2003). The model configuration mainly follows the default schemes and parametrisations for regional applications, and are summarised in Appendix A.1. Lateral advection of momentum and tracers (temperature and salinity) is computed with third-order upstream biased schemes, using a split and rotated formulation to limit diapycnal mixing, while vertical advection relies on a fourth-order compact scheme (Marchesiello et al., 2009; Lemarié et al., 2012). Subgrid-scale vertical mixing is represented with a K-profile parametrisation (KPP, Large et al., 1994), which accounts for surface and bottom boundary layer mixing, non-local transport in the surface layer, and interior mixing driven by shear instability and convection. The bottom drag coefficient is computed from a quadratic friction log-layer and a bottom stress limitation for stability.

To refine the resolution around each of the two regions of interest, the islands of Barbuda and Saint Martin, the model is used with its two-way nesting capabilities, provided by the Adaptive Grid Refinement in Fortran (AGRIF) package (Debreu et al., 2012). Both configurations share the same parent domain, which covers the northern Caribbean arc at a 3-km resolution, followed by two successive nested domain zooms at 600-m and 120-m resolution around each targeted island (Fig. 1). The bathymetry is constructed from the regional bathymetric digital elevation models of *Service Hydrographique et Océanographique de la Marine* (SHOM) Homonim project. The 0.005° resolution product (SHOM, 2017) is used for the 3-km parent grid domain, as well as the nested domains of Barbuda, while the 0.001° resolution product (SHOM, 2018; DOI: 10.17183/MNT_ANTN100m_HOMONIM_WGS84) is used for the two finer resolution domains of the Saint Martin configuration, as available on this area only. All domains have 32 vertically stretched levels, with stretching parameters (θ_s = 7 and θ_b = 2) providing enhanced resolution near the surface and the bottom, and a transition depth between the horizontal surface and the bottom terrain following levels, h_c = 200 m.

The parent domain is forced at its four open lateral boundaries with sea level, barotropic and baroclinic velocities, salinity, and temperature. To reduce small-scale effects and ensure a smooth transition between the model interior solution and boundary conditions, a sponge layer with enhanced viscosity and diffusivity is applied near the boundaries. Open boundary conditions are prescribed using a characteristics method for barotropic velocities, while radiative conditions are applied to baroclinic velocities, salinity and temperature (Marchesiello et al., 2001). Initial and lateral boundary conditions are derived from the daily mean of the global ocean reanalysis provided by the E.U. Copernicus Marine Service Information (CMEMS), with a horizontal resolution of 1/12° and 50 vertical levels (DOI: 10.48670/moi-00021). The simulations also include tidal forcing at the boundaries, processed with tidal sea level and current derived from Oregon State University's TPXO7 global ocean tide models (Egbert and Erofeeva, 2002), with a one-day ramp applied at initialisation.

Several experiments are conducted with various atmospheric fields and bulk formulations detailed in Section 2.3. Surface gravity wave effects on the modelled surge are not considered in the present study, which focuses on the sensitivity of storm surge to uncertainties in the characterisation and representation of the TC wind forcing. The chosen case study is not strongly impacted by wave setup given the geographical and morphological configuration, as discussed in Section 4. Each simulation is run using a 48-hour period (September 5 and 6, 2017), using baroclinic and barotropic time steps of 75 s and 1.5 s respectively. Sensitivity tests (not shown) confirm that the chosen time window is sufficient to eliminate the influence of initial adjustments on the surge evolution on September 6. Instantaneous outputs are saved hourly on September 5, and at 10-min intervals on September 6, when TC Irma made landfall on both islands.

2.3. Atmospheric forcings

The momentum, heat and water fluxes are computed within CROCO with the COARE 3.0 (Fairall et al., 2003) or ECUMEv6 bulk formulations (Roehrig et al., 2020) using 10-m wind speed, sea level pressure, 2-m air temperature and humidity, surface precipitation, and short and long wave radiation. Two atmospheric forcing strategies are employed in the simulations. The first one uses the European Centre for Medium-Range Weather Forecasts ERA5 (Hersbach et al., 2020) reanalysis provided at hourly frequency on a 0.25° grid for all the aforementioned variables. However, ERA5 is known to strongly underestimate TC intensities (e.g. Hodges et al., 2017; Dulac et al., 2024), by 37% in average for TC maximum wind intensities according to Jullien et al. (2024). For example, during the landfalls over Barbuda and Saint Martin on September 6, maximum winds reached 32 m.s^{-1} in ERA5, compared with 80 m.s^{-1} in IBTrACS. To overcome this strong underestimation of TC intensity, a second forcing strategy is thus preferred: while 2-m air temperature and humidity, surface precipitation, short and long wave radiation are still taken from ERA5, the wind and pressure fields are reconstructed using the approach proposed by Herry et al. (2025). It consists in blending a parametric TC model, driven by observed intensities, within the ERA5 reanalysis, providing the large-scale field around the TC. ERA5 wind and pressure fields are first filtered along the TC track to remove the too weak TC vortex. Then, best-track TC characteristics are used to build parametric radial profiles of the 10-m winds and surface pressure. Finally, these

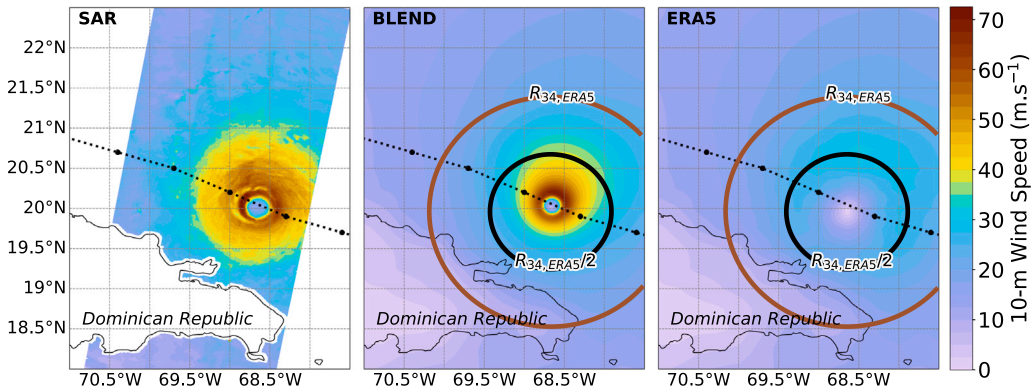

Fig. 2. Snapshots of the 2D wind field on September 7 at 10:30 UTC from SAR observations (left), the blended wind field (middle), and ERA5 reanalysis (right). ERA5 field, available hourly, is interpolated at the selected time. The track of TC Irma is shown as a black dotted line. The radii used in the blending procedure, $R_{34,ERA5}$ and $R_{34,ERA5}/2$, are indicated by brown and black circles, respectively.

parametric fields are blended with the filtered ERA5 fields using the 34-kt radius of maximum winds, usually used to characterise outer-wind TC size (e.g. Chavas and Knaff, 2022; Schenkel et al., 2023). A transition zone between $R_{34,ERA5}/2$ and $R_{34,ERA5}$ ensures a smooth transition between the parametric inner-core representation and the ERA5 winds in the outer-core region. Within $R_{34,ERA5}/2$ of the cyclone centre, the parametric wind field is added to the filtered ERA5, while beyond $R_{34,ERA5}$, the wind field corresponds solely to ERA5 winds. Further details on the method can be found in Appendix A.2 and in the reference paper by Herry et al. (2025). Overall, the authors showed that this procedure results in an enhanced representation of the maximum TC intensity and radial profile (wind and pressure), while preserving the spatial asymmetries and outer-wind large-scale structures provided by the global reanalysis, where it is reliable (Schenkel et al., 2017; Bian et al., 2021). Using Herry et al. (2025) toolbox (DOI: https://doi.org/10.12770/11057ae4-b708-481a-9848-2e4fdef57625), the 10-m winds and surface pressure fields are reconstructed on a 3-km grid to correctly represent Irma's wind and pressure forcing, and every 15 min to properly account for its motion. To be consistent with IBTrACS methodology, the interpolation is linear for maxima winds and radii, and spline for the TC position.

Fig. 2 illustrates the 2D wind fields from ERA5, the blended forcing, and SAR observations for TC Irma on September 7 at 10:30 UTC, i.e. when a SAR image was available. ERA5 markedly underestimates the maximum wind speed, reaching only 33% of the value observed in the SAR data. The blended forcing shows a much better agreement with observations with a realistic intensity and size, although the maximum wind is not located at the front but to the right of the TC, highlighting some limitations of the parametric representation. The blended forcing indeed reproduces the large-scale asymmetry of the synoptic flow, characterised by stronger winds on the TC right side (relative to its north-westward motion), but cannot represent localised small-scale asymmetries diverging from the general behaviour, such as that of the atypical front location of the maximum observed in the SAR data. Nevertheless, the reconstructed blended wind field provides a much more realistic forcing than ERA5.

2.4. Numerical experiments

A reference simulation, named REF, is conducted using the blended wind and pressure fields described in the previous section. For comparison, another simulation is performed using the native ERA5 fields (WPERA5). In order to evaluate the contribution of the atmospheric pressure gradient to the surge, two additional simulations are conducted: one not accounting for the TC-induced pressure drop by prescribing a constant 1000 hPa surface pressure (PatmCst), and another partially accounting for it by using the ERA5 original surface pressure (PatmERA5). Then, several numerical experiments are designed to assess the sensitivity of surge simulations to known uncertainties in TC atmospheric forcing, specifically (i) the wind intensity and wind-induced surface stress parametrisation, (ii) the spatial structure of the cyclonic wind field, and (iii) the spatio-temporal position of the TC centre. To that end, the blended wind field is reconstructed for several scenarios with modified TC intensity, structure, or position within the range of uncertainties given by IBTrACS observations. In addition to these TC characteristics, the surface stress strongly depends on the choice of the bulk parametrisation of air–sea fluxes for which large discrepancies exist under strong winds (>30 m.s^{-1}, Bryant et al., 2016). These differences reflect both the difficulty of obtaining reliable observations in such extreme conditions, and the dependence on the sea state. Several field measurements or laboratory experiments suggest a saturation or decrease of the drag coefficient at high wind speeds (e.g. Powell et al., 2003; Takagaki et al., 2012). Nonetheless, owing to its dependence on sea-state conditions that are not exclusively governed by wind speed, this parameter can potentially take significantly different values for the same wind intensity across different regions around the TC (Holthuijsen et al., 2012; Zhou et al., 2022). To explore the associated sensitivity, as wave effects are not explicitly represented in this study, two contrasting parametrisations are employed, chosen to span the upper and lower bounds of the aforementioned spread: ECUMEv6 (τECM, Roehrig et al., 2020), which features a pronounced decrease of the drag coefficient at high wind speeds, and COARE 3.0 (Fairall et al., 2003), in which the drag coefficient increases roughly linearly (see Appendix A.3). Besides the choice of the bulk parametrisation, sensitivity of the surge to wind-induced surface stress is partly due to uncertainty in the maximum wind speed, V_{max}, itself. Hence, the two aforementioned simulations are also carried out with the V_{max} input parameter, used to construct the wind and pressure fields, respectively reduced and increased by $\delta_{vm} \sim 3.6$ m.s^{-1} (7 kt), i.e. the IBTrACS V_{max} uncertainty, see Section 2.1. Uncertainties in TC atmospheric conditions also lie in the representation of the TC wind spatial structure. Indeed, an accurate representation of the entire TC vortex requires correctly capturing the radius of maximum wind, the decay rate of winds beyond this radius, as well as complex spatial patterns including asymmetries and localised features on scales of a few kilometres. To explore the surge sensitivity to some of these wind spatial characteristics, a simulation investigates variations of the radius of maximum wind by using the formulation of R_{max} from Willoughby et al. (2006) instead of that from Avenas et al. (2023) used in REF (see formulations in Appendix A.2). Another simulation uses a different parametric wind profile formulation $V(r)$ to assess the impact of the radial wind structure. The Willoughby et al. (2006) formulation is used instead of that of Wood et al. (2013). These two formulations differ on how they represent the wind speed decay beyond the radius

Table 1
List and characteristics of the sensitivity numerical experiments. For each experiment, the type of atmospheric forcing is given, with further specification when the sources of wind and atmospheric pressure (Patm) are distinct. The wind stress formulation used is also indicated. For experiments using parametric fields, the model inputs, R_{max}, V_{max}, and the TC longitude (lon) and latitude (lat), are specified. HE25 refers to Herry et al. (2025), AV23 to Avenas et al. (2023), OL17 to Olfateh et al. (2017), and IBTrACS is abbreviated as BT. For each experiment, parameters that differ from REF are shown in bold.

Experiment	Atmo. forcing	R_{max}	V_{max}	TC position	Wind stress
REF	HE25	AV23	BT	BT	COARE
WPERA5	**ERA5**	–	–	–	COARE
PatmCst	Winds: HE25 **Patm: 1000 hPa**	AV23	BT	BT	COARE
PatmERA5	Winds: HE25 **Patm: ERA5**	AV23	BT	BT	COARE
TrackLAT+	HE25	AV23	BT	lon_{BT} $\mathbf{lat_{BT} + \delta_{tr}}$	COARE
TrackLAT−	HE25	AV23	BT	lon_{BT} $\mathbf{lat_{BT} - \delta_{tr}}$	COARE
TrackLON+	HE25	AV23	BT	$\mathbf{lon_{BT} + \delta_{tr}}$ lat_{BT}	COARE
TrackLON−	HE25	AV23	BT	$\mathbf{lon_{BT} - \delta_{tr}}$ lat_{BT}	COARE
τECM	HE25	AV23	BT	BT	**ECUME**
Vmax+REF	HE25	AV23	$\mathbf{BT+\delta_{vm}}$	BT	COARE
Vmax−REF	HE25	AV23	$\mathbf{BT-\delta_{vm}}$	BT	COARE
Vmax+ECM	HE25	AV23	$\mathbf{BT+\delta_{vm}}$	BT	**ECUME**
Vmax−ECM	HE25	AV23	$\mathbf{BT-\delta_{vm}}$	BT	**ECUME**
RmaxWi06	HE25	**WI06**	BT	BT	COARE
ModelWi06	**Winds: WI06** Patm: HE25	AV23	BT	BT	COARE
AsymOlf17	HE25 + **asym. OL17**	AV23	BT	BT	COARE

of maximum wind, enabling an exploration of its impact on surge simulations. Finally, a simulation is conducted in which TC asymmetry is not represented by the ERA5 background field within $R_{34,ERA5}/2$ but is instead prescribed by the formulation proposed by Olfateh et al. (2017), fitted to SAR data by Vinour et al. (2025) (see formulations in Appendix A.2). Beyond $R_{34,ERA5}/2$, the same methodology as described in Section 2.3, and used in REF, is applied.

Lastly, to assess the impact of spatio-temporal uncertainty in TC position on storm surge simulations, four experiments are carried out with modified tracks, obtained by shifting the IBTrACS track by $\pm\ \delta_{tr} = 10$ km (Category-5 positional uncertainty ranges between 10–15 km, see Section 2.1), either in latitude with fixed longitude (TrackLAT±) or in longitude with fixed latitude (TrackLON±). This simplified method does not capture the full complexity of track uncertainties, which are neither uniform nor systematic, but preserves a realistic track shape and provides a reasonable basis for sensitivity analysis.

All simulations characteristics are summarised in Table 1.

2.5. Data and metrics for model evaluation

Modelled and observed storm surges are expressed as free surface anomalies (i.e. including tides), defined as deviations from the mean pre-surge total sea level on September 5. Simulated surges are compared with tide gauge observations from both islands. At Saint Martin, we use 1-minute measurements from the harbour tide gauge (63.085°W, 18.083°N) operated by the Collectivity of Saint Martin and available through the SHOM data portal. At Barbuda, we use 6-minute data from the NOAA tide gauge (61.821°W, 17.591°N), retrieved from UNESCO's sea level station monitoring facility. The location of both tide gauges are shown as black crosses in Fig. 1. The raw data are processed with an interquartile range filter to remove outliers. The observed and simulated surges are analysed according to three main criteria: the maximum surge amplitude (max. η), the timing (t_p) and duration of the peak surge (Δp). This latter parameter is defined as the time interval during which the surge amplitude exceeds 25% of the observed

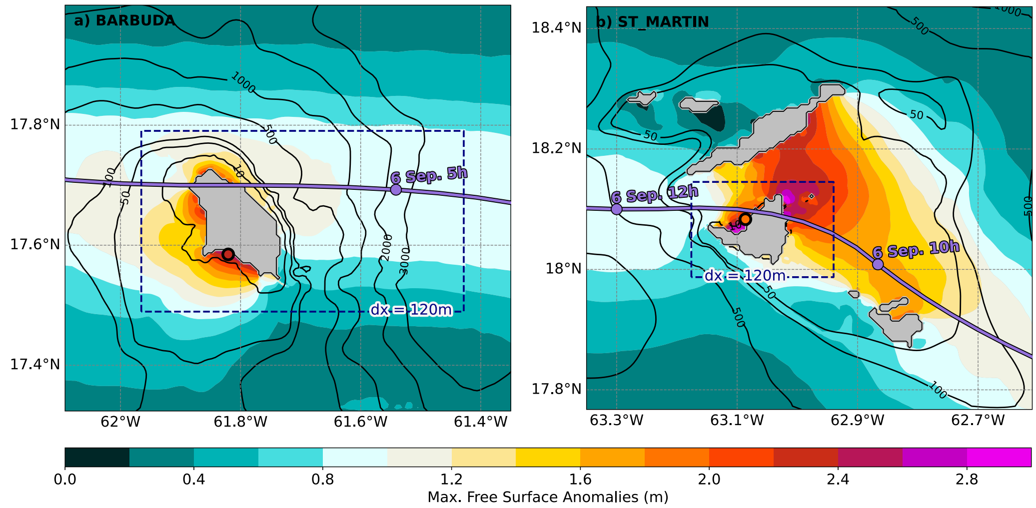

Fig. 3. Maximum free surface anomalies on September 6 in the REF simulation around Barbuda (a) and Saint Martin (b). Dashed blue lines represent the finer nest (dx = 120 m) boundaries. The two dots, coloured by the maximum observed free surface anomalies, indicate the locations of the tide gauges (where the simulation is compared with observations). Modelled iso-depth are indicated with black lines, labelled in metres, and Irma's track is the purple line.

maximum within the considered simulation period, i.e. September 5–6, 2017. The events studied here are characterised by narrow and intense surge peaks (Fig. 4). Using a relative threshold based on observations ensures a consistent reference across all sensitivity experiments and allows us to detect whether such peak is actually reproduced in the simulations. Percentile-based thresholds are sensitive to dataset length and would require long, consistent, and thoroughly quality-controlled observational records. A threshold of 25% of the observed maximum was empirically selected instead, after a sensitivity analysis, as it represents a compromise between including a sufficient number of observed and modelled points, while remaining restrictive enough to isolate the surge peak. The surge peak metrics are compared between the simulations and the observations or between sensitivity experiments and a reference simulation through the bias or relative bias $rbias$, defined as:

$$\begin{cases} bias = E - R \\ rbias = \frac{bias}{R} \times 100 \end{cases} \quad (1)$$

where R and E denote the reference and the considered experiment values, respectively.

3. Results

3.1. Model validation

Fig. 3 presents the maximum surge simulated in the reference experiment (REF) around both islands. At Saint Martin, the modelled surge exceeds one metre over the tens of kilometres of the continental shelf with a depth inferior to 50 m surrounding the island. Very large values exceeding 2.6 m extend to the north and north-east of the island, locally reaching more than 2.8 m in the bay where the tide gauge is located. At Barbuda, the areas most exposed to the surge are located to the west and, in particular, the south-west of the island, where the modelled surge reaches 2.6 m. The western side of Barbuda exhibits gentler depth gradients than the eastern side, but remain sharper than around Saint Martin, resulting in a more limited spatial extent of high surge values. In both cases, the tide gauges are positioned within or nearby the regions affected by the highest simulated surge.

Time series of the modelled storm surge at the two tide gauges (Fig. 4, top panels) show that at Saint Martin, the reference experiment accurately reproduces the timing of the surge peak, as well as the rising slope leading up to it. The maximum amplitude of the surge is overestimated (2.35 m instead of the observed 2.00 m, rbias of 18%, Table 2), although this overestimation is short, lasting only about 30 min, due to the sharp and narrow shape of the peak. A stronger than observed secondary peak is modelled around 11:30 UTC, as well as a strong negative peak around 12:00 UTC, which is not observed at the tide gauge, and induces a 1 h shorter peak duration. At Barbuda, the maximum amplitude and timing of the surge, as well as the post-peak decrease are well reproduced. However, the simulation produces a narrower peak surge duration (1 h instead of the observed 2h20, Table 2).

The wind time series at the tide gauge locations (Fig. 4, bottom panels) exhibit the characteristic signature of a TC, with two wind speed maxima, corresponding to the passage of the two eyewalls, separated by a smaller wind speed, corresponding to the passage of the TC eye. This pattern is more clearly defined at Saint Martin, consistent with the TC track passing closer to that tide gauge. At Saint Martin, the wind intensity reaches 68 $m.s^{-1}$ and the surge peak coincides with the first eyewall passage, while the subsequent negative surge corresponds to the second eyewall passage. At Barbuda, the wind reaches 63 $m.s^{-1}$ and the surge maximum corresponds to the second eyewall passage.

Discrepancies between modelled and observed surges may arise from various sources, including errors in the TC track that affect both the TC intensity and the local wind direction near the tide gauges, inaccuracies in the wind field structure and asymmetries due to limitations in the constructed blended forcing, which has a limited capability to represent TC asymmetry and cannot capture local wind effects such as orographic effects. To a lesser extent, uncertainties and biases in the tide gauge measurements, as well as model limitations, may also contribute to the observed discrepancies, and are discussed in Section 4. Despite these uncertainties and limitations, the reference simulation, forced by a parametric vortex embedded in ERA5, proves adequate for reproducing the key surge characteristics and appears sufficiently accurate for conducting sensitivity analyses exploring some of the aforementioned factors. In contrast, the simulation forced by the native ERA5 forcing (WPERA5) strongly underestimates the surge, with no marked peak and relative biases of −82% and −81% at Saint Martin and Barbuda, respectively. It never exceeds the 25% threshold of the observed maximum amplitude used for defining the peak duration. This substantial underestimation can be attributed to ERA5 large underestimation of TC intensity associated to its coarse spatial resolution. As shown in Fig. 4, the ERA5 wind forcing exhibits maximum wind speeds reaching only 25 $m.s^{-1}$, and considerably smoother gradients compared with the reference simulation.

Table 2
Biases of key metrics of the REF and WPERA5 simulations with respect to observations. For the peak maximum (max. η), the relative biases are also indicated into brackets.

Experiment	Location	Max. η (cm)	t_p (min)	Δp (min)
REF	Barbuda	8 (3%)	2	−80
	Saint Martin	35 (18%)	9	−60
WPERA5	Barbuda	−191 (−81%)	128	–
	Saint Martin	−163 (−82%)	19	–

Table 3
Biases of key metrics of the REF and PatmERA5 simulations with respect to PatmCst. For the peak maximum (max. η), the relative biases are also indicated into brackets.

Experiment	Location	Max. η (cm)	Δ_p (min)	t_p (min)
REF	Barbuda	43 (21%)	20	0
	Saint Martin	48 (26%)	80	0
PatmERA5	Barbuda	20 (10%)	80	0
	Saint Martin	22 (12%)	30	0

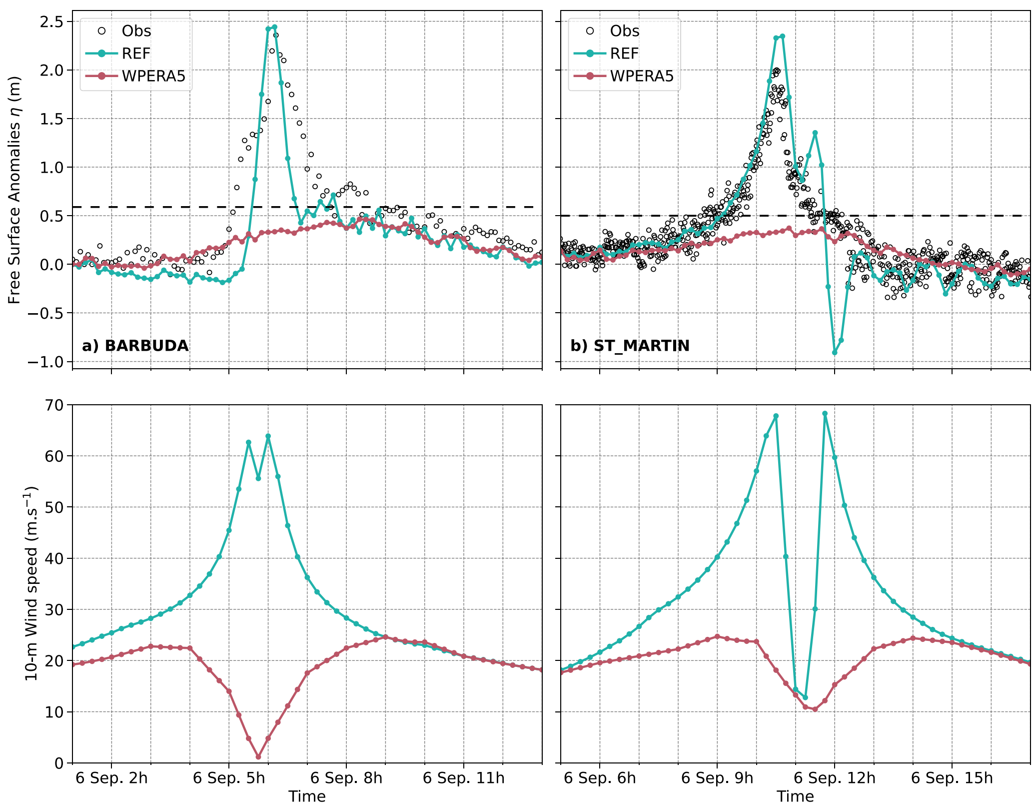

Fig. 4. Time series of free surface anomalies η (top, m) and 10-m wind speed (bottom, m.s^{-1}) at (a) Barbuda and (b) Saint Martin for the REF simulation (cyan) and the WPERA5 simulation (pink) at the grid point closest to each tide gauge. Observations are shown as black dots. The threshold corresponding to 25% of the observed maximum η, used to define the surge peak duration, is shown as black dashed lines in top panels.

3.2. Impact of atmospheric pressure gradient to the modelled surge

The contribution of the atmospheric pressure gradient to the modelled surge is assessed by comparing a simulation in which a uniform surface pressure (sp) of 1000 hPa is imposed (PatmCst), with the reference simulation (REF). A simulation with the blended wind field but ERA5 pressure field (PatmERA5) is also conducted to assess the respective impacts of ERA5 underestimation of the pressure drop and wind intensity.

When comparing PatmCst to REF (Fig. 5 and Table 3), surface pressure differences reach up to −80 hPa and −60 hPa at Saint Martin and Barbuda tide gauges, respectively, resulting in corresponding differences in free surface anomalies of up to 1 m and 0.6 m. These results are consistent with the inverse barometer rule, which states that a 1 hPa pressure decrease drives an increase in sea level of about 1 cm (e.g. Wunsch and Stammer, 1997). The timing of minimum pressure, where the pressure contribution to the surge is strongest, is slightly shifted from the timing of the maximum peak surge, which occurs in phase with one of the TC eyewall passages. Hence, the atmospheric pressure gradient adds 48 cm in the surge peak maximum at Saint Martin, and 43 cm at Barbuda. This contribution drops to 22 cm and 20 cm when considering PatmERA5. The atmospheric pressure gradient also extends the duration of the surge peak by 20 min at Barbuda and 1h20 at Saint Martin.

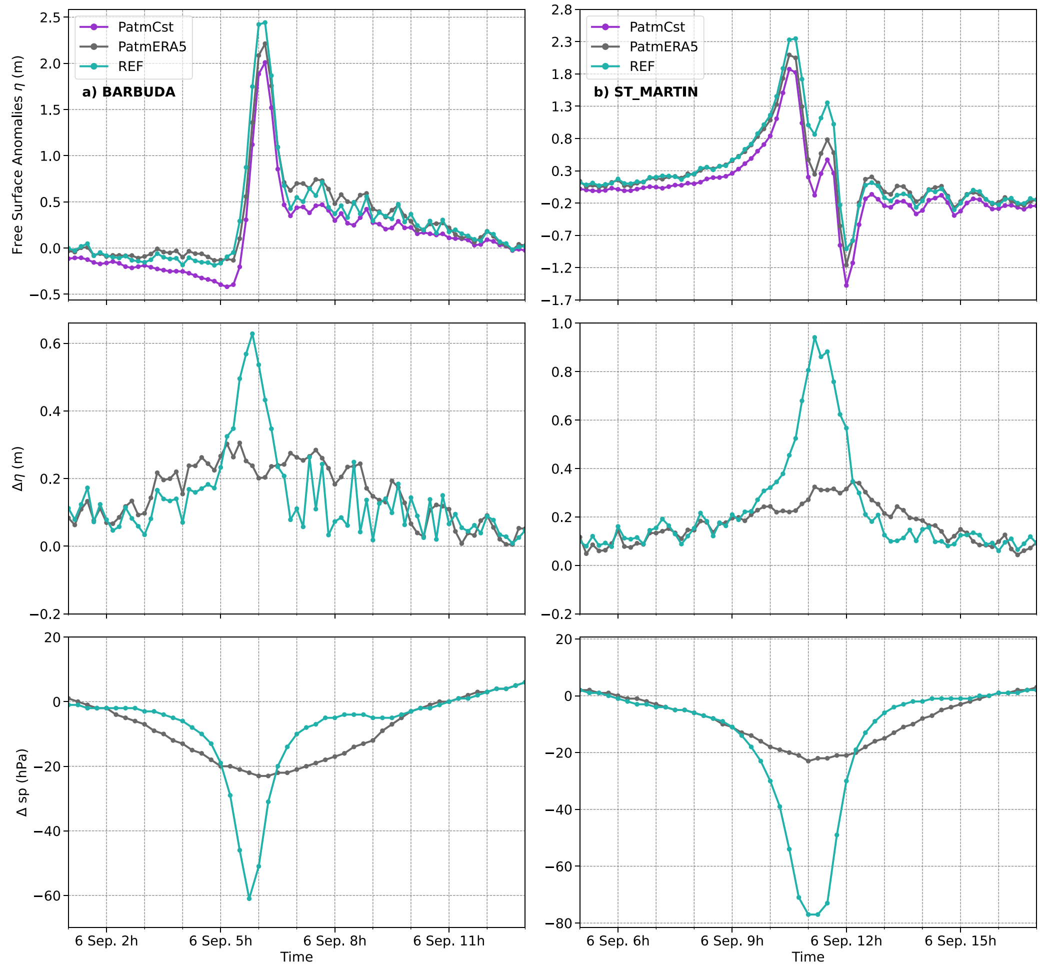

Fig. 5. Time series of free surface anomalies η (top, m) at (a) Barbuda and (b) Saint Martin for the REF (cyan), PatmCst (purple), and PatmERA5 (grey) simulations. Middle and bottom panels depict the differences in free surface anomalies and surface pressure relative to PatmCst, respectively.

Table 4
Biases of key metrics of modified-track simulations with respect to REF. For the peak maximum (max. η), the relative biases are also indicated into brackets.

Experiment	Location	Max. η (cm)	Δp (min)	t_p (min)
TrackLON+	Barbuda	7 (3%)	−10	−20
	Saint Martin	−10 (−4%)	0	−30
TrackLON−	Barbuda	16 (7%)	0	10
	Saint Martin	−1 (0%)	0	20
TrackLAT−	Barbuda	0 (0%)	−10	10
	Saint Martin	−31 (−13%)	−40	10
TrackLAT+	Barbuda	−108 (−44%)	−10	0
	Saint Martin	−39 (−17%)	0	−10

3.3. Sensitivity to TC spatio-temporal position

The sensitivity of storm surge modelling to best-track uncertainties in TC position is then assessed by comparing scenarios with modified tracks (TrackLON± and TrackLAT±), shown in Fig. 6 a–b, to the reference simulation REF. Fig. 6 c–h show their associated time evolution in terms of modelled wind stress, surface pressure, and resulting free surface anomalies at the tide gauge locations, while Table 4 shows the biases of each simulation with respect to REF. Latitude shifts mainly affect the intensity of all fields, whereas longitude shifts primarily alter their timing (up to 30 min), consistently with the predominant east–west orientation of Irma's track. At Saint Martin, the relative difference in peak surge amplitude from REF reaches up to −17% (max. η = 1.96 m for TrackLAT+, compared with max. η = 2.35 m for REF). Latitude-shifted experiments (TrackLAT+ and TrackLAT−) no longer exhibit the secondary maximum present in REF near 11:30 UTC. Furthermore, all simulations except TrackLAT+ produce a strong negative surge, though not supported by the observations. This strong negative surge appears in phase with the second wind stress peak and is discussed later. At Barbuda, the sensitivity of surge maximum amplitude to TC position is even more pronounced, with a relative difference reaching up to −44% for TrackLAT+.

These large variations in surge amplitudes are directly linked to associated strong sensitivities of the simulated wind stress and surface pressure (Fig. 6 e–h). As the cyclone passes very close to the tide gauge locations and is characterised by sharp gradients in pressure and wind, even small shifts in the track substantially modify the local TC intensity. The eyewall-eye-eyewall wind stress pattern (2 peaks separated by a

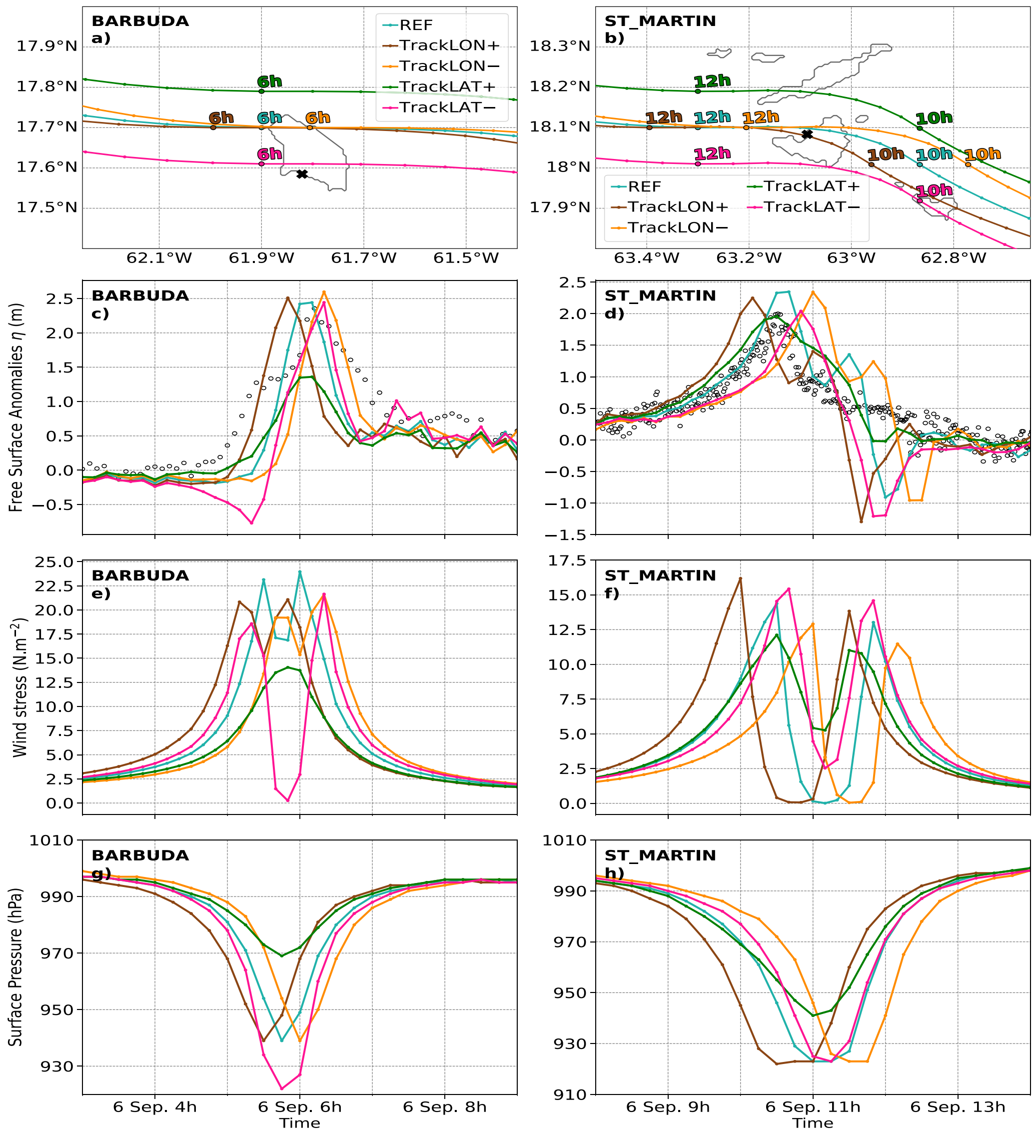

Fig. 6. Surge sensitivity to TC track at Barbuda (left column; panels a, c, e, g) and Saint Martin (right column; panels b, d, f, h). The reference simulation (REF) is shown in cyan, while the various track-modified simulations are in brown (TrackLON+), orange (TrackLON−), pink (TrackLAT−), and green (TrackLAT+). The upper panels (a, b) display Hurricane Irma's track for each simulation, with tide gauge locations indicated by black crosses. The lower three rows show time series of free surface anomalies (m; panels c, d) including observations (black dots), wind stress (N.m^{-2}; panels e, f), and surface pressure (hPa; panels g, h).

calmer period, Fig. 6 e–f) is strengthened as the TC passes closer to the tide gauges (TrackLON+ at Saint Martin, TrackLAT− at Barbuda), while being less pronounced and even changing to a bell-shape (TrackLAT+ at Barbuda) when the TC passes more far away, as the eyewall misses the tide gauge site, explaining the largely reduced peak surge amplitude. Track perturbations also modify the minimum surface pressure modelled at the tide gauge locations, with differences reaching up to +18 hPa and +30 hPa for TrackLAT+ at Saint Martin and Barbuda, respectively. These results illustrate that modelling surge very close to a TC track is highly sensitive to uncertainties in TC position, even when only shifting the track by a few kilometres.

To better understand the modifications of the modelled surge induced by track shifts, particularly the formation of the secondary maximum and the negative surge at Saint Martin, snapshots of the free surface anomalies between 10:00 and 12:00 UTC are examined for REF, TrackLAT+ and TrackLAT− (Fig. 7). The spatial pattern of the surge appears to be influenced by the presence of Anguilla island (Fig. 1), which blocks the water flow, promoting accumulation in the channel between the two islands. This accumulation, combined with strong onshore winds associated with the first eyewall passage, explains the maximum modelled surge in the bay where the tide gauge is located. In REF, the secondary maximum occurs when the eye passes over the channel. The associated sudden drop in the wind forcing may generate oscillations in water levels constrained by Anguilla, whereas in TrackLAT−, the eye passes south of the channel, which therefore remains continuously exposed to strong winds. A preliminary test (not shown) indicates that the secondary peak is indeed no longer modelled when Anguilla is removed from the simulation. Since this pattern is less pronounced in observations, it may suggests that the actual cyclone track was slightly shifted relatively to IBTrACS data, as TrackLAT− does not reproduce this feature. Cécé et al. (2021) indeed reported that the track observed by radar and satellite measurements, as well as that simulated by a dynamical atmospheric model, was slightly more southerly than that reported in IBTrACS during Irma's passage over Saint Martin. Further investigations will be required to fully understand this secondary peak pattern. The negative surge in REF is associated with strong north-westward wind stress offshore the northern coast of Saint Martin (Fig. 7). In TrackLAT−, this negative surge is further

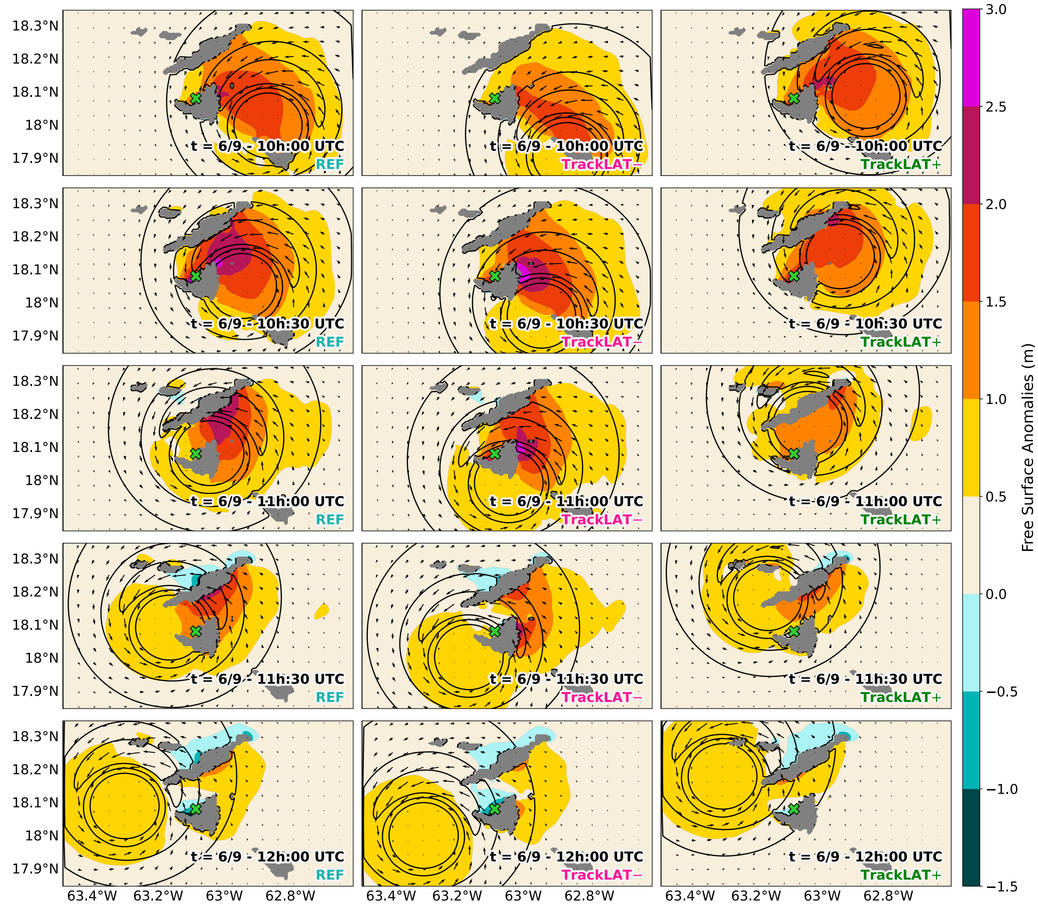

Fig. 7. Snapshots of free surface anomalies for REF (left), TrackLAT− (middle), and TrackLAT+ (right) simulations around Saint Martin every 30 min between 10:00 and 12:00 UTC on September 6 (each row represents one time). The tide gauge is shown as a green cross, wind stress contours (every 10 N.m^{-2}) as black lines, and wind speed with arrows indicating magnitude and direction.

enhanced by winds oriented even more to the north-west. In contrast, in TrackLAT+, the wind stress is weaker and directed northward, thus less favourable to the generation of a negative surge.

The sensitivity of surge amplitude to track variations is also evident, and can be even more pronounced at the island scale, as illustrated by the differences in maximum free surface anomaly between each latitude-modified simulation and REF (Fig. 8). Hence, at Saint Martin, although the various experiments lead to variations of less than 50 cm in peak surge at the tide gauge location (Table 4), the maximum surge along the north-eastern coast varies by 0.75–1 m when latitude-modified tracks (TrackLAT±) are considered. In TrackLAT−, such variations reflect a higher maximum surge in this region, that was already part of the most exposed area with more than 2.6 m of maximum surge (Fig. 3b). At Barbuda, differences relative to REF exceeding 1 m are found near the tide gauge location for TrackLAT+. In the north-west of Barbuda, variations of the same order of magnitude are obtained for TrackLAT−, while differences of more than 50 cm are found for TrackLAT+. These results show that slight modifications of the TC track, while remaining within the range of best-track uncertainties, can significantly alter which regions of the islands are exposed to high surge conditions.

3.4. Sensitivity to wind intensity and surface stress

Next, we evaluate the sensitivity of the modelled surge to current limitations in the wind-induced surface stress representation, including both diverse wind stress parametrisations and best-track wind intensity uncertainties. To that end, the REF simulation is compared with a simulation using the ECUMEv6 bulk parametrisation (τECM) instead of COARE 3.0, and 4 simulations with modified maximum winds (either increased or decreased by 3.6 m.s^{-1}) with both the COARE 3.0 and ECUMEv6 parametrisation (Vmax±REF and Vmax±ECM). The two parametrisations produce markedly different wind stress behaviour for wind speeds exceeding 30 m.s^{-1} (see Fig. A.16 in Appendix A.3).

Fig. 9 and Table 5 reveal that modelled surge peak amplitude is very sensitive to wind-induced surface stress, while this parameter have little to no effect on surge peak duration and timing. At the tide gauge locations, replacing COARE 3.0 with ECUMEv6 reduces the maximum wind stress by more than four times. This leads to weaker wind stress gradient during the TC passage and in turn simulated maximum surges are reduced by more than 50% in τECM compared with REF (1.14 m against 2.35 m at Saint Martin, 1.16 m against 2.44 m at Barbuda). The observed maxima (2.00 m and 2.36 m at Saint Martin and Barbuda, respectively) lie between those two values, being however much closer to REF. At Saint Martin, the smoother wind stress gradient in τECM delays and limits the surge rise and almost removes the negative surge during the second eyewall passage. The primary and secondary positive peaks tend to merge into a single, broader but weaker maximum. This stress-parametrisation sensitivity is modulated by the sensitivity to prescribed wind intensity. The maximum surge is modulated by 8%–15% around REF, and by 2%–10% around τECM when modifying the maximum winds according to the best-track uncertainty range. The effect is more pronounced around REF, consistently with the stronger dependence of wind stress on wind speed in COARE 3.0 parametrisation. The larger wind stress induced difference, considering both maximum wind and parametrisation sensitivity together (i.e. between REF and Vmax−ECM), is −56% at Saint Martin, and −55% at Barbuda.

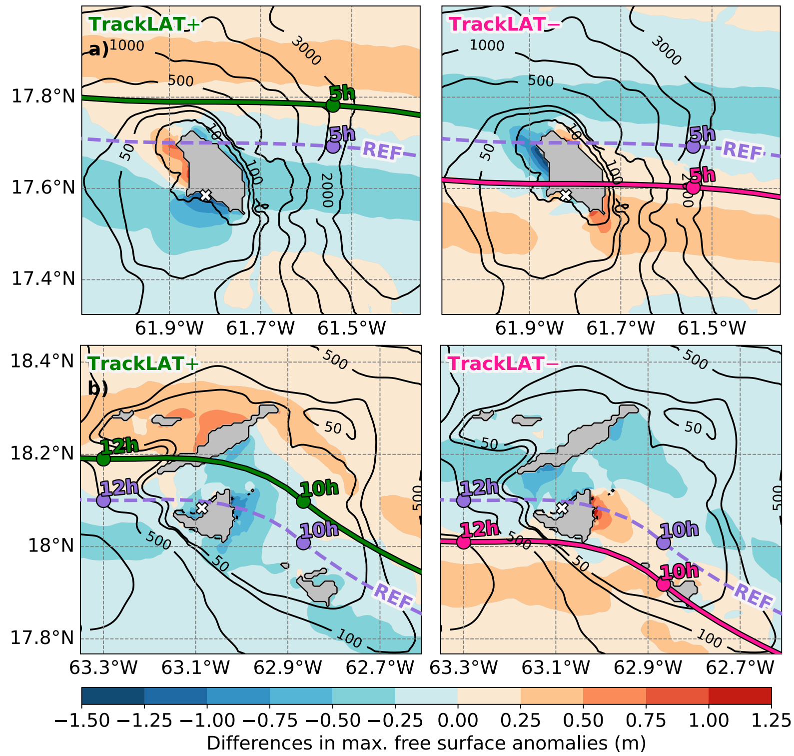

Fig. 8. Differences in maximum free surface anomalies between the latitude-modified simulations and REF around (a) Barbuda and (b) Saint Martin on September 6. The left (right) panels show differences with TrackLAT+ (TrackLAT−), with the corresponding TC track indicated by green (pink) line, and associated dates on September 6. In each panel, the dashed purple line shows the REF track, white crosses indicate the locations of the tide gauges, and modelled iso-depth are shown as black contour lines, labelled in metres.

Table 5
Biases of key metrics of stress-modified simulations with respect to REF. For Vmax±ECM, biases relative to τECM are also shown in italics. For the peak maximum (max. η), the relative biases are indicated into brackets.

Experiment	Location	Max. η (cm)	Δp (min)	t_p (min)
τECM	Barbuda	−128 (−52%)	−10	−10
	Saint Martin	−121 (−51%)	−40	10
Vmax−ECM	Barbuda	−133 (-55%)	−10	−10
		−5 (−4%)	*0*	*0*
	Saint Martin	−132 (−56%)	−40	10
		−11 (−10%)	0	0
Vmax+ECM	Barbuda	−126 (−52%)	−10	−10
		2 (2%)	*0*	*0*
	Saint Martin	−111 (−47%)	−40	10
		10 (9%)	*0*	*0*
Vmax−REF	Barbuda	−20 (−8%)	0	0
	Saint Martin	−25 (−11%)	0	−10
Vmax+REF	Barbuda	22 (9%)	0	−10
	Saint Martin	36 (15%)	−10	0

Fig. 10 shows that each tide gauge is located within or nearby the regions exhibiting the highest sensitivity, consistent with the spatial pattern of maximum surges in REF (Fig. 3). The effect of variations in the maximum wind intensity is less extended than that of changing the wind stress parametrisation. The latter shows differences exceeding 60 cm between REF and τECM along most of the northern and western coasts of Barbuda, as well as in the channel between Saint Martin and Anguilla. As expected, since the contribution of wind stress to surge generation is inversely proportional to water depth, regions of high sensitivity to wind stress correspond to shallow areas, such as the continental shelf, with depths inferior to 50 m, between Saint Martin and Anguilla.

3.5. Sensitivity to TC wind structure

Finally, to explore the sensitivity of surge modelling to uncertainties in TC wind structure, REF is compared with 3 modified-structure simulations: RmaxWi06 with a modification of the R_{max} formulation, ModelWi06 with a modification of the parametric formulation, and

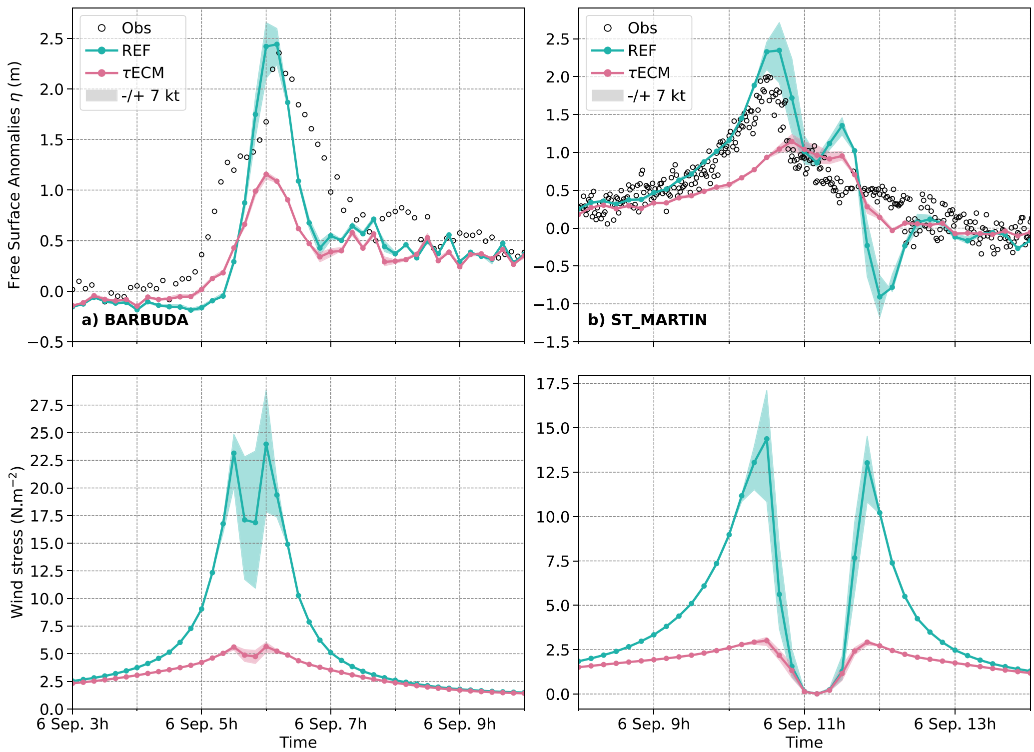

Fig. 9. Time series of free surface anomalies (m, top) and wind stress ($N.m^{-2}$, bottom) at Barbuda (a) and Saint Martin (b) for REF in cyan and for τECM in pink. Shading respectively represents the maximum intensity–modified simulations Vmax±REF and Vmax±ECM. Observed free surface anomalies are shown as black dots.

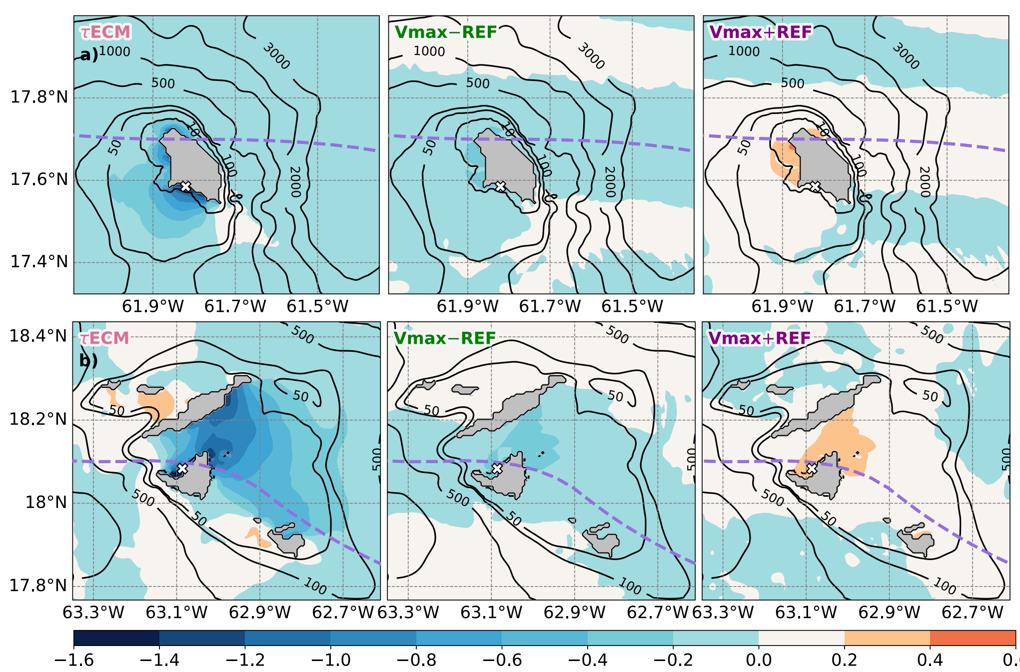

Fig. 10. Differences in maximum free surface anomalies between the simulation with modified wind stress parametrisation (τECM) or maximum TC intensity (Vmax±REF), and REF around (a) Barbuda and (b) Saint Martin on September 6. Each panel shows differences for a given simulation. The TC track is indicated by a dashed purple line, tide gauge locations by white crosses, and modelled iso-depth by black contour lines, labelled in metres.

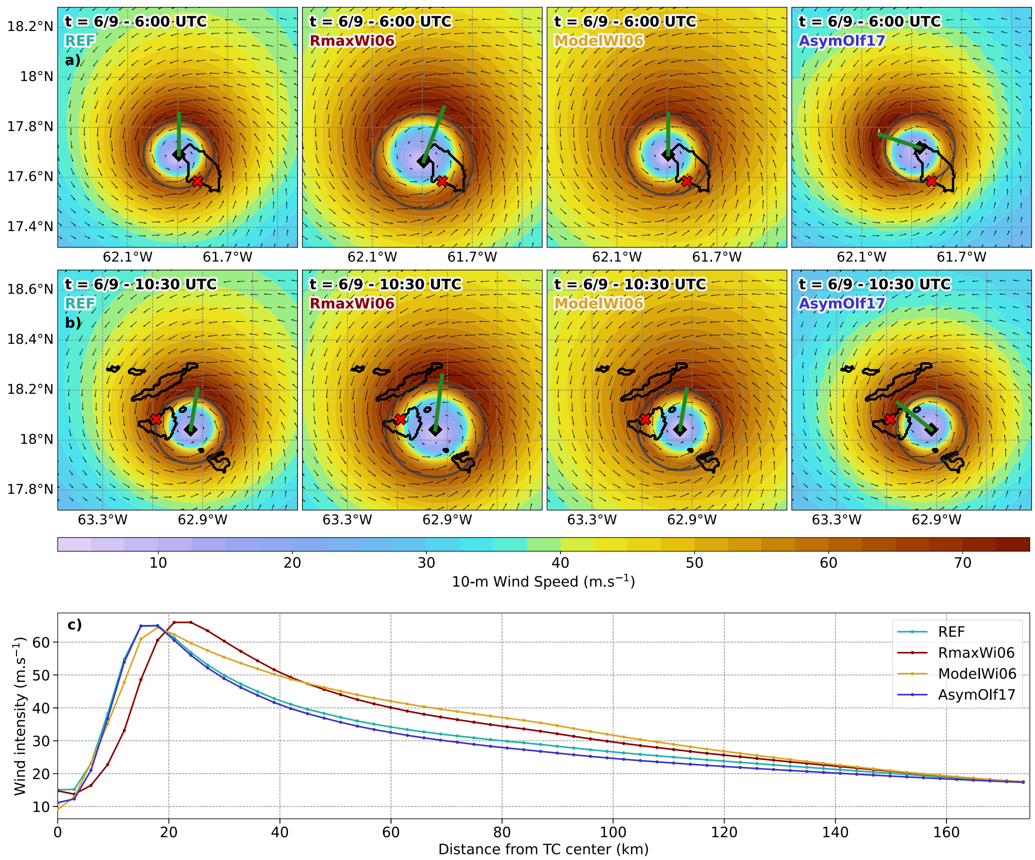

Fig. 11. Comparison of 10-m winds used for the REF and modified-structure simulations. Top and middle panels show 2D 10-m wind fields on September 6 during Irma's passage over Barbuda (06:00 UTC, a) and Saint Martin (10:30 UTC, b). The green line and black circle indicate the 2D radius of maximum winds and the azimuthally averaged R_{max}, respectively. Tide gauge locations are indicated with red crosses. The bottom panel (c) shows the mean radial wind profiles on September 6.

Table 6
Biases of key metrics of the structure-modified simulations with respect to REF. For the peak maximum (max. η), the relative biases are also indicated into brackets.

Experiment	Location	Max. η (cm)	Δp (min)	t_p (min)
RmaxWi06	Barbuda	16 (7%)	90	10
	Saint Martin	3 (1%)	50	−20
ModelWi06	Barbuda	−9 (−4%)	90	0
	Saint Martin	−15 (−6%)	30	−10
AsymOlf17	Barbuda	−13 (−5%)	−10	−10
	Saint Martin	25 (11%)	−10	0

AsymOlf17 with a modification of the asymmetry. Fig. 11 first compares their wind field and profile. Next, the associated simulated surge and differences relative to REF are shown at the two tide gauge locations in Fig. 12 and Table 6, while Fig. 13 presents the differences in maximum surge around both islands.

The R_{max} formulation of Willoughby et al. (2006) used in RmaxWi06 produces a larger mean R_{max} than that of Avenas et al. (2023) used in REF (24 km against 18 km, Fig. 11c). For comparison, IBTrACS reports a slightly larger R_{max} of 28 km, though this estimate is imprecise, with errors larger than 30% for Category-5 cyclones (Combot et al., 2020). Although these differences in R_{max} are only a few kilometres, they induce marked discrepancies in the associated wind fields, with extended area under high winds or under the calm of the eye. At Saint Martin, the peak surge occurs about 20 min earlier in RmaxWi06, consistently with the larger R_{max} causing strong onshore winds to reach the tide gauge slightly earlier, and last overall longer (+50 min in Δp, Fig. 12, Table 6). At Barbuda, the surge decay is slightly delayed (in better agreement with observations). While the surge amplitude at the two tide gauges is only weakly affected by the change in R_{max} (absolute differences with REF up to 16 cm, Table 6), the sensitivity is more pronounced in other areas around the studied islands (Fig. 13). At Saint Martin, the larger R_{max} in RmaxWi06 leads to maximum surge values exceeding those in REF by up to 50 cm along the northeastern coast of Anguilla and the southeastern coast of Barbuda.

The wind profile decay in ModelWi06, using Willoughby et al. (2006) rather than Wood et al. (2013) parametric formulation, is less steep than that of REF, and also leads to an extended area under high winds (with absolute differences in wind profile of up to 8 m.s^{-1}, Fig. 11), and an extended surge duration (+30 and +90 min for Saint Martin and Barbuda tide gauges respectively, Fig. 12 and Table 6). The slower wind field decay in ModelWi06 exhibits a weaker spatial impact, although the western coast of Barbuda generally experiences a slight decrease in maximum surge (10–30 cm) compared with REF (Fig. 13).

Finally, exploring the impact of the parametric wind asymmetry, the AsymOlf17 simulation, which exhibits a more pronounced asymmetry than REF, and a maximum wind located in the TC front rather than

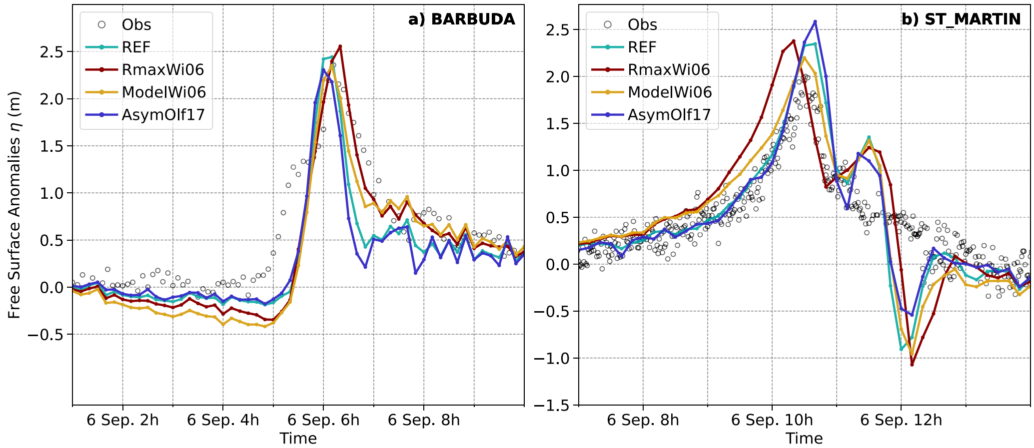

Fig. 12. Time series of free surface anomalies (m) at Barbuda (a) and Saint Martin (b) for the REF (cyan), RmaxWI06 (red), ModelWI06 (yellow), and AsymOlf17 (dark blue) simulations. Observed free surface anomalies are shown as black dots.

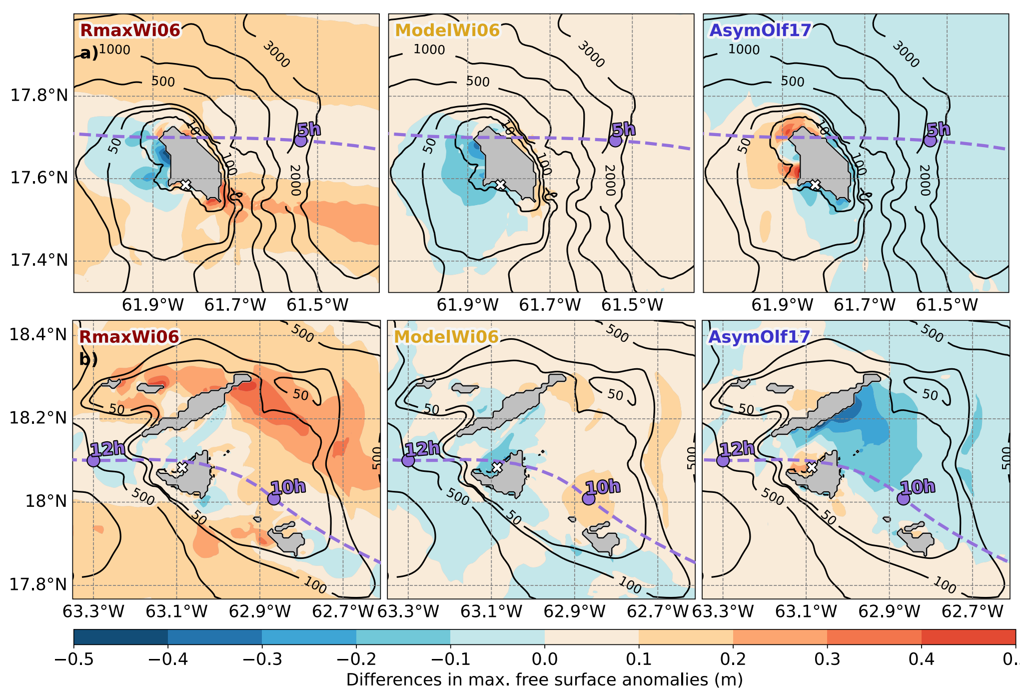

Fig. 13. Differences in maximum free surface anomalies between the structure-modified simulations (RmaxWI06, ModelWI06, and AsymOlf17) and REF around (a) Barbuda and (b) Saint Martin on September 6. Each panel shows differences for a given simulation. The TC track is indicated by a dashed purple line, tide gauge locations by white crosses, and modelled iso-depth by black contour lines, labelled in metres.

to its right (Fig. 11), induces a higher maximum surge at Saint Martin tide gauge (2.60 m vs 2.35 m for the REF simulation) but a weaker negative peak surge (Fig. 12 and Table 6). At Barbuda tide gauge, the cyclone being slightly farther from the tide gauge location, the impact is weaker and mostly lies in a slightly reduced peak duration (−10 min). However, at the islands scale, changed asymmetry in AsymOlf17 produces reductions of 30–40 cm in maximum surge along the southern coast of Anguilla and similar increases along parts of the northwestern coast of Barbuda, compared with REF (Fig. 13).

Overall, these results show that, given the small size of the islands of Barbuda and Saint Martin (diameters of 10–25 km), the wind distribution during the TC landfall is very sensitive to TC the structure (broadness, shape of the wind decay, location of stronger winds). At the two tide gauges, these differences mainly affect surge duration. Although the surge amplitude sensitivity is smaller in magnitude than that associated with wind stress or TC track variations, changes in TC structure noticeably modify the exposed areas.

4. Discussion

While using ERA5 wind and pressure fields leads to a major underestimation of the modelled surge (∼ −80% for the peak amplitude) at Saint Martin and Barbuda tide gauges, using a blended forcing with realistic intensity produces substantially better results. These results are

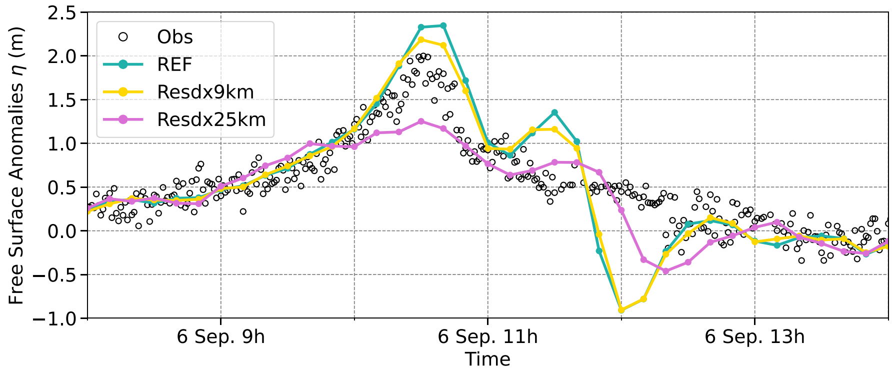

Fig. 14. Time series of modelled free surface anomalies at Saint Martin for the reference simulation REF (cyan), Resdx9km (yellow), and Resdx25km (pink). Observations are shown as black dots.

consistent with Echevarria et al. (2026), in which parametric TC forcing outperforms atmospheric reanalysis in simulating surges but contrast with those of Chaigneau et al. (2024). Atmospheric forcing resolution is a key factor controlling the representation of the TC structure and the associated surge response (Ridder et al., 2018; Agulles et al., 2024), and ERA5, given on a 0.25° resolution grid, is known to strongly underestimate TC maximum winds (e.g. Hersbach et al., 2020; Jullien et al., 2024; Herry et al., 2025). In contrast, the blended wind field, used in all other simulations, is constrained with observed maximum intensity (which cannot be solved by ERA5), and provided on a finer grid resolution (0.027°). Contrary to the results obtained here, Dullaart et al. (2020) showed that ERA5 performed well in simulating storm surges induced by Irma in Florida, even at locations where the TC track passed very close to tide gauges. However, Florida is surrounded by a wide continental shelf, allowing the surge to accumulate towards the coastline, whereas Saint Martin and Barbuda have much narrower shelves. In addition, Irma impacted Florida at a lower intensity, as a Category-4 in the Florida Keys, and as a Category-3 in south-west Florida (Cangialosi et al., 2021), while, in the studied case, the eyewall of a Category-5 hurricane directly passed over the tide gauges. Taken together, these factors reduce the sensitivity of the surge response to the underestimation of TC maximum intensity, which may explain the performance of ERA5 in Dullaart et al. (2020). Similarly, Chaigneau et al. (2024) reported better surge simulations using ERA5 forcing than parametric models for Irma. The same arguments applied for the surges along Florida coasts. Other locations considered in their study were situated in Puerto Rico or in the U.S. Virgin Islands, several tens of kilometres from the TC centre. With more moderate winds at these locations, ERA5's underestimation of peak intensity has a smaller impact on the simulated surges. Moreover, outside the TC inner core, ERA5 may provide more realistic wind fields than stand-alone parametric models, as it assimilates available observations and can better represent large-scale asymmetries. The forcing we have used in our study has the advantage of using ERA5 winds in the TC periphery, and a parametric formulation only in the inner-core, where the winds are the strongest, and where those from ERA5 are strongly underestimated (Herry et al., 2025).

As the structure of the wind and pressure fields can also vary depending on the resolution of the grid they are represented on, it also appeared interesting to evaluate the impact of the chosen atmospheric forcing grid. Observational means have various spatial resolutions (e.g. radiometers, scatterometers and SAR observations have resolutions on the order of 40, 25 and 1 km, respectively), and besides representing the accurate maximum wind, we have shown that the wind structure plays an important role. To explore the sensitivity of the simulated surge to the grid interpolation smoothing, two additional experiments were conducted with the same parameters used to construct REF wind and pressure fields, but interpolated onto coarser grids of 9 km (Resdx9km) and 25 km (Resdx25km), instead of the 3-km grid used in REF. The resulting free surface anomalies at Saint Martin (Fig. 14) highlight a marked dependence of the surge peak on the resolution of the atmospheric forcing, with maximum amplitudes decreasing from 2.35 m in REF, to 2.19 m in Resdx9km, and 1.25 m in Resdx25km. The much larger reduction observed for Resdx25km compared with Resdx9km suggests the existence of a resolution threshold beyond which interpolation-induced smoothing severely degrades the representation of the parametric fields. These results underline the necessity of conducting sensitivity analyses before using such parametric forcings in ocean models, in order to identify an optimal compromise between resolution, and therefore computational and storage costs, and an acceptable level of degradation in the simulated TC fields.

Despite its relatively high resolution, the blended field still exhibits limitations in its representation of TC atmospheric conditions, which are reflected in the simulated storm surge. Indeed, although blending with ERA5 introduces some asymmetry, the overall TC structure remains largely idealised, being based on an azimuthally averaged wind profile, whereas real cyclones exhibit a much more complex and asymmetric wind field (see for instance the 2D wind speed from SAR in Fig. 2). Small-scales wind structures exist due to the internal variability of the TC or its interaction with external forcings such as flow shear, ocean gradients, or land. In particular, when a TC crosses land, its overall intensity decreases due to the loss of its oceanic heat source, and the increase in surface roughness (Chen and Chavas, 2020). This effect is considered in a few parametric wind formulations (Kaplan and DeMaria, 1995; Boose et al., 2004; DeMaria et al., 2006; O'Grady et al., 2024). In the studied case, both islands are small relatively to the size of the cyclonic vortex, making the TC only briefly and partially exposed to land. The effect may thus be limited. However, the increase in surface roughness impacts the asymmetry of the landfalling system, leading to lower wind speeds over land than over the ocean (O'Grady et al., 2024), while land use and orography may further locally enhance or reduce TC wind speeds or gusts (Chambers and Li, 2011; Barbary et al., 2019; Cécé et al., 2021). In particular, Cécé et al. (2021) showed that Saint Martin's topography induced localised gust speed-up zones during Irma. At Saint Martin, orographic effects could have a significant influence on TC winds, as the island is relatively mountainous, with Paradise Peak reaching more than 400 m above sea level (Institut national de l'information géographique et forestière (IGN) classical map). Depending on the wind orientation towards or from the land (first and second eyewall respectively), we may expect different land-related effects on the wind field especially at tide gauge coastal location. In particular, these missing effect may explain the strong negative surge modelled in REF but not observed at the tide gauge. Indeed, this negative surge coincides with the second eyewall passage, and no attenuation was applied in the blended forcing to account for the reduction of offshore winds after crossing the mountainous region, and just before reaching the tide gauge. Similar strong negative surge following the surge peak were also simulated with parametric TC winds in Echevarria et al. (2026), and were attributed to an oversimplified treatment of land effects on wind speed. To assess the potential impact of wind attenuation over land, preliminary sensitivity experiments (not shown) were conducted, in which winds were reduced over land as suggested in previous studies (Kaplan and DeMaria, 1995; Boose et al., 2004; DeMaria et al., 2006; O'Grady et al., 2024) by attenuation factors ranging from 0.6 to 0.8. We also extended the land-induced reduction to winds over the coastal ocean when winds blew offshore linearly or exponentially over distances of 5 to 50 km offshore. These experiments revealed that local wind attenuation substantially reduces the amplitude of the modelled negative surge as the second eyewall passes over Saint Martin, with reductions ranging from 30 cm to 1 m, depending on the considered strength and spatial extent attenuation. However, the positive surge peak was also attenuated in these experiments, likely due to the 3-km resolution of the atmospheric forcing relative to Saint Martin spatial length scale of 10–15 km, and the proximity of Anguilla island. Further work is needed to better account for the complexity of the TC wind field, and in particular for representing orographic or land-use effects in such islands. A dynamical atmospheric model could offer more complex and finer wind fields (e.g. Cécé et al., 2021), but comes with a high computational cost and other issues, such as the inherent stochasticity of TC that may hinder the exact reproduction of observed spatial structures. For TC Irma, an additional difficulty lies in accurately representing its rapid intensification before landfall on the two studied islands (DeMaria et al., 2021; Torgerson et al., 2023).

It can also be noted that the present study has not considered wave related processes. Those may influence the water level in several ways. A first effect could be related to their potential impact on the wind stress, as several studies showed that explicitly accounting for the dependence of surface stress on sea state, through wind stress parametrisation integrating wave age or wave-induced stress, can improve storm surge modelling (e.g. Mastenbroek et al., 1993; Bertin et al., 2015; Pineau-Guillou et al., 2020). However, no consensus has yet emerged and multiple formulations coexist, none of which being well constrained at high wind speeds, and furthermore for winds approaching 80 m.s^{-1}, i.e. the intensity of TC Irma during its landfall on both islands. The parametrisations used in the present study (Appendix A.3) cover the overall range of existing parametrisations even if not explicitly accounting for sea state variability for a given wind intensity. Another wave-induced effect could be associated to wave–current interactions that might enhance bottom friction stress (Nicolle et al., 2009; Wu et al., 2018). Finally, wave dissipation in the nearshore could induce a wave setup that may reach several tens of centimetres during storms (Kennedy et al., 2012; Lavaud et al., 2020). Nonetheless, resolving this process requires grid resolutions of the order of tens of metres to properly represent the surf zone. In the present study, the objective was neither to quantify the relative contributions of the different physical processes to the studied surges nor to be able to reproduce observations as closely as possible, but to investigate the influence of current limitations in the representation of TC wind-forcing on storm surge modelling. Hence, accounting for waves would introduce additional sources of uncertainty and make it more difficult to isolate the specific impact of various wind forcing scenarios on the simulated surge. Moreover, the tide-gauge locations, relative to the TC track, make them relatively sheltered from wave exposure. At Saint Martin, Rey et al. (2019) showed that significant wave height did not exceed 3 m at the entrance of the bay where the tide gauge is located, with the most wave-exposed areas being the eastern and southeastern coasts. Preliminary tests (not shown) using a coupled hydrodynamic-wave model also confirmed that wave-related contributions to the studied surge are much smaller than atmospheric contributions.

Finally, part of the discrepancies between observed and modelled surge levels may also arise from uncertainties and biases in tide gauge measurements or model limitations. Although recent tide gauge observations are generally capable of achieving cm to mm-level accuracy (Martin Miguez et al., 2012; Woodworth et al., 2016; Pytharouli et al., 2018) they remain affected by multiple sources of error, including changes in sensor reference, clock de-synchronisation or positional drift. These can manifest as linear trends, abrupt offsets, or gradual drifts, and may lead to biases, typically on the order of ± 15 cm, if not properly corrected (Martin Miguez et al., 2012; Pytharouli et al., 2018). Such biases are particularly critical for long-term trend analyses, or when absolute water level value is required, but not in an event case like this study. Meanwhile, in situ measurements of sea level during extreme events can be challenging and may result in missing data at the surge peak or offsets following the event. Although not explicitly labelled as fully validated by the data provider, the high-frequency tide gauge datasets used here appeared to be of reliable quality, and capture surge levels exceeding 2 m. They are therefore especially valuable for such extreme surge study. Another potential source of discrepancy in model-data comparison is representativeness of the model grid point versus that of the tide gauge. As in other studies (e.g. Chaigneau et al., 2024), we performed comparisons using the nearest model grid point to each tide gauge, but this point may not necessarily be the most representative of local conditions. Alternative approaches, such as spatial averaging over a given radius (e.g. Agulles et al., 2024) or selecting the least biased grid point within a neighbourhood (e.g. Dullaart et al., 2020), have been proposed to reduce this representativeness error. The tide gauges are located in sheltered environments, where they capture highly localised dynamics that are unlikely to be fully resolved, even at the relatively fine model resolution used here (120 m), further contributing to the observed discrepancies. A sensitivity test including an additional nest at 40-m resolution was then performed and showed that the simulated surges converge towards the results obtained with the 120-m nest, indicating that the chosen resolution adequately resolves the considered surge. Bathymetry also represents a critical input for accurate storm surge modelling (e.g. Weaver and Slinn, 2010; Paugam et al., 2021). Nevertheless, in this study, the bathymetric dataset used for Saint Martin has a higher resolution than the model grid. The 500-m resolution bathymetry used around Barbuda may introduce some uncertainty in the modelled surge, although, to the best of our knowledge, no finer dataset is currently available. Overall, the limitations described above are considered to remain acceptable, as the agreement between modelled and observed surge levels is sufficient for the purpose of this study, which focuses on analysing relative differences between sensitivity experiments rather than achieving the closest possible fit to observations.

5. Conclusion

In early September 2017, Category-5 Hurricane Irma made landfall on the narrow islands of Barbuda and Saint Martin, inducing significant storm surges, captured by each island's tide gauge located only a few kilometres away from the TC centre. This study investigates the sensitivity of the modelled surges to variations in TC atmospheric characteristics. Surges simulations are conducted using a two-way nested configuration of the CROCO ocean model, forced with a state-of-the-art parametric wind formulation, fitted to best-track observations, and blended with the ERA5 background flow (Herry et al., 2025). The parametric vortex, as well as the wind stress formulation, is then carefully adjusted to explore the influence of a posteriori uncertainties in track position, wind intensity, surface stress, and horizontal wind structure, on the simulated surges. It should be noted that using ERA5 wind forcing fields alone leads to a substantial underestimation of peak surges, with values about five times lower than observed. These weak predictive skills are attributed to the coarse resolution of ERA5, its substantial underestimation of Irma's intensity, and the specific location of the studied sites, just under Irma's strongest winds.

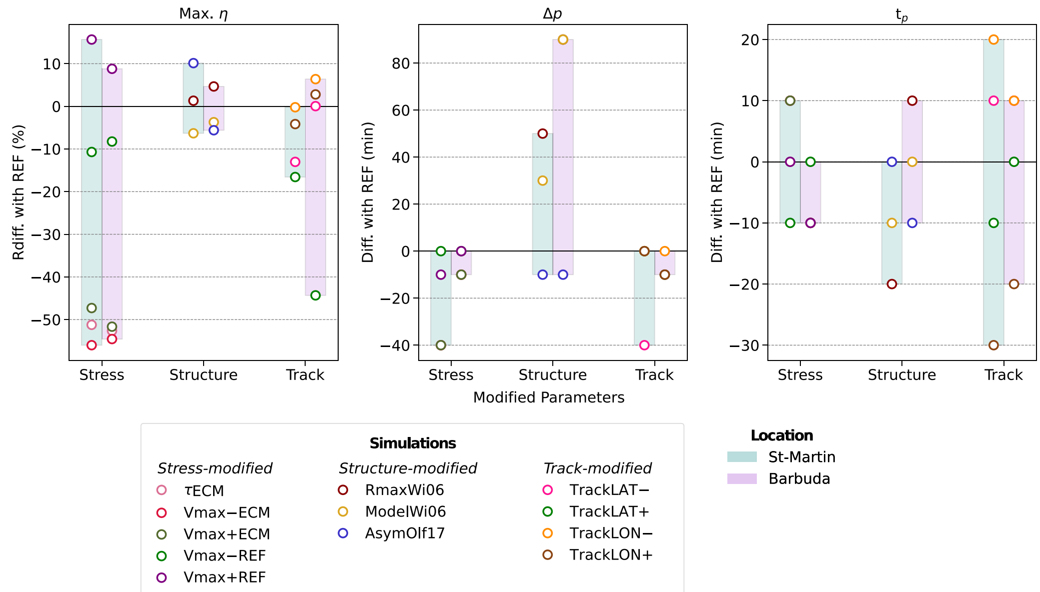

Fig. 15. Summary of all stress-, structure- and track-modified experiments forced with the blended wind forcing. For each experiment, the peak surge amplitude (max η, left), duration (Δp, middle), and timing (t_p, right) are compared against the corresponding metrics in REF. The panels show the difference (diff) between each experiment and REF for peak duration and timing, and the relative difference (rdiff) for peak surge amplitude. For each category of experiments, the range of (relative) differences is shown as an envelope, cyan for Saint Martin, and purple for Barbuda. Inside these envelopes, each experiment is plotted as a coloured dot.

The results of all sensitivity experiments with the blended wind field are synthesised in Fig. 15, which shows the (relative) differences in peak surge metrics between each experiment and the reference simulation, REF. Overall, the modelled surge is highly sensitive to the variations in TC wind conditions (i.e. track, structure, intensity, or wind stress). The surge amplitude can vary up to 56% relatively to the reference simulation with the largest contribution to this sensitivity lying in the choice of the wind stress parametrisation (51%–52%) at both sites, further enhanced by variations in the prescribed wind intensity. Shifts of 10 km in the track position can lead to surge variations of up to 44% at Barbuda, while the duration of the surge is more strongly controlled by the horizontal wind structure, with increases of up to 1h30. A strong site-dependency of surge variations to track and wind structure is however highlighted: at Saint Martin, amplitude variations remain below 20% in track-modified experiments, and peak timing differences are limited to about 50 min in structure-modified experiments. The small size of the considered islands, the proximity of the tide gauges to the TC track, the high intensity of Irma, and the location of the studied sites in relatively steep bathymetry areas, likely all contribute to a strong response of modelled storm surge to variations in the TC wind forcing.

This study highlights the importance of accounting for uncertainties in the TC wind forcing when analysing modelled storm surges, as variations within the range of uncertainty of key TC characteristics, even a posteriori to the event, can lead to large, highly case-specific differences in the resulting surge. The same methodology, assessing cyclone-specific uncertainties followed by targeted sensitivity experiments, could be applied to other surge hindcasts, providing practical guidelines for future modelling studies. Evaluating the sensitivity of surge modelling to these uncertainties is essential to better characterise the hazard, assess the contributions of different physical processes to the surge, and develop more effective coastal risk management or adaptation strategies. In the context of surge forecasting, such an evaluation is even more critical, as TC wind forcing uncertainties are even larger, and assessing the associated range of possible surges can help improve informed decision for emergency responses.

CRediT authorship contribution statement

A. Zribi: Writing – original draft, Visualization, Software, Investigation, Conceptualization. **S. Jullien:** Writing – review & editing, Supervision, Conceptualization. **N. Herry:** Writing – review & editing, Software, Resources. **X. Bertin:** Writing – review & editing, Supervision, Conceptualization. **G. Dodet:** Writing – review & editing, Supervision, Conceptualization.

Declaration of competing interest

The authors declare that they have no known competing financial interests or personal relationships that could have appeared to influence the work reported in this paper.

Acknowledgements

This work was supported by the French State under the PPR FUTURISKS Project, ‘Un Océan de Solutions’, managed by the National Research Agency, under France 2030 [grant No. ANR-22-POCE-0002] and by the SPC-Climate-FLAGSHIP project. The researchers were supported by the French National Institute for Ocean Science (Ifremer) for A.Z, S.J. and G.D., the French National Research Institute for Sustainable Development (IRD) for N.H. and the National Centre for Scientific Research (CNRS) for X.B. The simulations were performed using the supercomputer Datarmor and HPC resources of Ifremer's Centre for Computing and Data for the Sea. The authors also acknowledge the three anonymous reviewers for their constructive comments, which helped to improve the manuscript.

Appendix

A.1. CROCO schemes

See Table A.7.

A.2. Detailed methodology to construct the blended forcing

To overcome the strong underestimation of TC intensities in global reanalyses (Hodges et al., 2017), the wind forcing strategy follows the approach of Herry et al. (2025). It consists in blending a parametric TC model, driven by observed intensities, within a global reanalysis providing the large-scale wind field around the TC. This blended product adjusts the radial wind profile formulation $V(r)$ of Wood et al. (2013):

$$V(r) = V_0 + (V_{max} - V_0)\frac{\eta^{\lambda}\left(\frac{r}{R_{max}}\right)^{\kappa}}{\left(\eta - \kappa + \kappa\left(\frac{r}{R_{max}}\right)^{\eta/\lambda}\right)^{\lambda}} \quad \text{(A.1)}$$

where V_{max} and V_0 denote, respectively, the azimuthally averaged maximum wind speed, and the wind speed at the centre of the TC. The parameters κ, λ, and η control the sharpness, broadness, and decay rate of the profile. Along with V_0, they are estimated using a parametrisation, obtained after fitting the parametric model on SAR observations, as detailed in Herry et al. (2025), and reproduced in the following Eqs. (A.2). Finally, R_{max} corresponds to the azimuthally averaged radius of maximum wind.

$$\begin{cases} \kappa = 1.887 - 1.291 \cdot 10^{-5} R_{max} + 2.216 \cdot 10^{-2} V_{max} + 7.686 \cdot 10^{-3} |\phi| \\ \lambda = 0.677 - 3.261 \cdot 10^{-6} R_{max} + 2.387 \cdot 10^{-5} V_{max} - 7.839 \cdot 10^{-4} |\phi| \\ \mu = -0.787 - 2.071 \cdot 10^{-6} R_{max} - 2.623 \cdot 10^{-3} V_{max} + 1.903 \cdot 10^{-3} |\phi| \\ V_0 = 4.805 - 3.186 \cdot 10^{-5} R_{max} + 7.927 \cdot 10^{-2} V_{max} + 1.019 \cdot 10^{-1} |\phi| \end{cases} \quad \text{(A.2)}$$

Alternatively, the Willoughby et al. (2006) formulation for the wind parametric profile is used:

$$\begin{cases} V(r) = V_{max}\left(\frac{r}{R_{max}}\right)^{n}, r \le R_{max} \\ V(r) = V_{max}\left[(1-A)\exp\left(-\frac{r-R_{max}}{X_1}\right) + A\exp\left(-\frac{r-R_{max}}{X_2}\right)\right], r > R_{max} \end{cases} \quad \text{(A.3)}$$

The expression of the parameters A, n and X_1, which are dependent of V_{max}, R_{max}, and the latitude ϕ can be found in Willoughby et al. (2006), and are reproduced in the following Eqs. (A.4), while X_2 is a fixed parameter, equal to 25 km in this study.

$$\begin{cases} X_1 = 287.6 - 1.942 V_{max} + 7.799 \ln R_{max} + 1.819\phi \\ n = 2.1340 + 0.0077 V_{max} - 0.4522 \ln R_{max} - 0.0038\phi \\ A = 0.5913 + 0.0029 V_{max} - 0.1361 \ln R_{max} - 0.0042\phi \end{cases} \quad \text{(A.4)}$$

The value of R_{max} is estimated using the formulation proposed by Avenas et al. (2023):

$$R_{max} = \frac{V_{max}}{f}\left(\sqrt{1 + \frac{2 f M_{max}}{V_{max}^2}} - 1\right) \quad \text{(A.5)}$$

where f is the Coriolis parameter and M_{max} is the angular momentum at R_{max}. This latter quantity is inferred from statistical relationships, derived from radiometer observations, between angular momentum and wind radii at 34- (R34), 50- (R50), and 64 kt (R64), as described in Avenas et al. (2023) and reproduced hereafter:

$$\begin{cases} \frac{M_{max}}{M_{34}} = 0.531 \cdot e^{-0.00214(V_{max}-17.5) - 0.00314(V_{max}-17.5)\left(\frac{1}{2} f R_{34}\right)} \\ \frac{M_{max}}{M_{50}} = 0.626 \cdot e^{0.00282(V_{max}-25.7) - 0.00724(V_{max}-25.7)\left(\frac{1}{2} f R_{50}\right)} \\ \frac{M_{max}}{M_{64}} = 0.612 \cdot e^{0.00946(V_{max}-32.9) - 0.01183(V_{max}-32.9)\left(\frac{1}{2} f R_{64}\right)} \end{cases} \quad \text{(A.6)}$$

Alternatively the formulation from Willoughby et al. (2006) is also used (R_{max}^{Wi}). This expression is simpler as it only depends on the maximum wind speed and the latitude ϕ, rather than outer wind radii:

$$R_{max}^{Wi} = 46.4 \cdot e^{-0.0155 V_{max} + 0.00169|\phi|} \quad \text{(A.7)}$$

The large-scale background field is provided by the European Centre for Medium-Range Weather Forecasts ERA5 reanalysis (Hersbach et al., 2020), with hourly surface wind fields on a 0.25° grid, covering the period from 1940 to the present. Following the Herry et al. (2025) procedure and associated toolbox (https://doi.org/10.12770/11057ae4-b708-481a-9848-2e4fdef57625) to blend this large-scale wind field to the parametric one, an 11-day low-pass filter is applied within a 200 km radius around the TC track, in order to remove the underestimated vortex core. The filtered ERA5 field is then blended with the parametric TC wind field using the 34-kt radius of maximum winds, usually used to characterise outer-wind TC size (e.g. Chavas and Knaff, 2022; Schenkel et al., 2023). The extent of the transition zone is adapted to the TC size and intensity, ensuring a smooth transition between the parametric inner-core representation and the ERA5 winds in the outer-core region. The azimuthally averaged 34-kt wind radius derived from ERA5 ($R_{34,ERA5}$) is used to define this transition, as Herry et al. (2025) showed that this radius is well reproduced when compared with high-resolution SAR surface wind observations. Within $R_{34,ERA5}/2$ of the cyclone centre, the parametric wind field is added to the filtered ERA5, while beyond $R_{34,ERA5}$, the wind field corresponds solely to ERA5 winds. Between these two radii, the datasets are smoothly merged. Sensitivity tests conducted by Herry et al. (2025), using different extents of the transition zone, or a fixed zone instead of a criterion based on $R_{34,ERA5}$, show that this configuration provides

Table A.7
List of CPP-keys specified in CROCO that define the numerical schemes used in REF, and detailed in Section 2.2.

Category	CPP-keys
Parallelisation	MPI
Nesting	AGRIF_2WAY
Open Boundary Conditions (OBC)	OBC_[EAST, WEST, NORTH, SOUTH] OBC_[M2CHARACT, M3ORLANSKI, TORLANSKI]
Grid configuration	CURVGRID; SPHERICAL; MASKING NEW_S_COORD
Model Dynamics	SOLVE3D; UV_COR; UV_ADV
Equation of state	SALINITY; NONLIN_EOS
Lateral forcing	[Z, M2, M3, T]_NUDGING [Z, M2, M3, T]_FRC_BRY
Surface forcing	BULK_FLUX; FORMATTED; READ_PATM
Advections	UV_HADV_UP3; UV_VADV_SPLINES TS_HADV_RSUP3; TS_VADV_SPLINES
Sponge layer	SPONGE
Bottom friction and forcing	LIMIT_BSTRESS ANA_[BSFLUX, BTFLUX]
Vertical Mixing	LMD_[MIXING, SKPP, BKPP] LMD_[RIMIX, CONVEC, NONLOCAL]
Tides	TIDES, [SSH, UV, POT]_TIDES; TIDERAMP

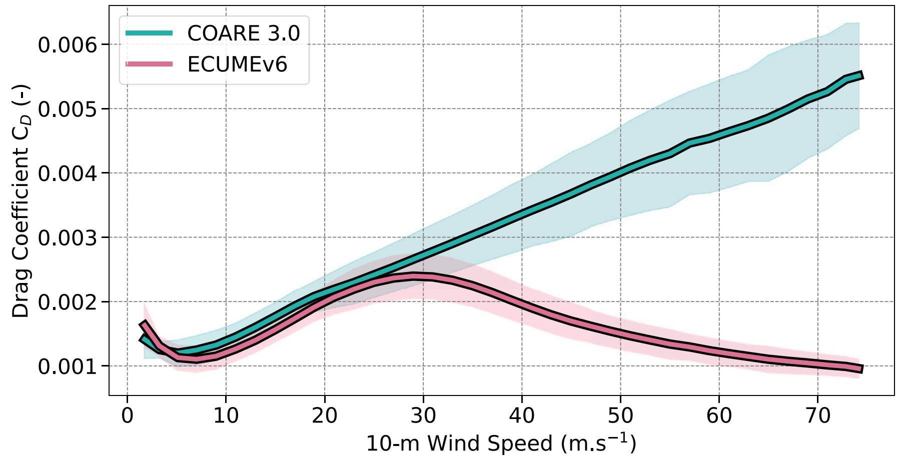

Fig. A.16. Effect of the COARE 3.0 and ECUMEv6 wind-stress parametrisations on the drag coefficient. For each 2 m.s^{-1} bin, the mean value over the 3-km simulation grid is shown (solid curves), together with the standard deviation (shaded areas).

the best agreement with SAR observations, thereby limiting errors associated with the blending parameters.

Alternatively, the parametric formulation of asymmetry proposed by Olfateh et al. (2017) is used, instead of using the one given by ERA5 background field. The resulting asymmetric wind profile, $V_a(r,\theta)$, is therefore defined as the sum of the symmetric wind profile, $V(r)$, and an asymmetric component, such as:

$$\begin{cases} V_a(r,\theta) = V(r) + \epsilon V_{\mathrm{WN1}}(r)\sin(\theta + sign(\phi)\beta) \\ V_{\mathrm{WN1}}(r) = \left[\exp(1)\cdot \frac{R_a^D}{r}\cdot \exp\left(-\frac{R_a^D}{r}\right)\right]^{\frac{1}{2}} \end{cases} \tag{A.8}$$

where $V_{\mathrm{WN1}}(r)$ is the first mode of asymmetry, β is the azimuth of the asymmetric maximum wind, multiplied by the sign of latitude ϕ, ϵ is the factor that determines the degree of asymmetry, R_a is the distance from the centre at which the asymmetry is maximum, and D adjusts the shape of the asymmetry radial profile. Regressions for these parameters are given in Vinour et al. (2025) and summarised hereafter:

$$\begin{cases} \beta(r) = \min\left(0,\ 156.1 - 185.6\frac{r}{R_{max}}\right) \text{ if } r < 1.2R_{max} \\ \beta(r) = -54.1 - 3.5\frac{r}{R_{max}} \text{ if } r \geq 1.2R_{max} \\ \epsilon = 3.26\times10^{-1} - 2.89\times10^{-3}V_{max} - 3.30\times10^{-2}\ln(R_{max}) + 8.30\times10^{-3}V_T \\ \ln(R_a) = 5.91\times10^{-1} - 1.50\times10^{-2}V_{\max} + 9.26\times10^{-1}\ln(R_{max}) + 4.92\times10^{-2}V_T \\ D = 9.30\times10^{-1} - 4.16\times10^{-3}V_{max} + 2.55\times10^{-1}\ln(R_{max}) - 2.37\times10^{-2}V_T \end{cases} \tag{A.9}$$

where V_T is the TC translation speed.

The TC pressure field is also reconstructed, following the wind–pressure relationship described by Knaff and Zehr (2007), as adapted in Herry et al. (2025). These fields take into account the characteristics of the previous reconstructed wind field, the position of the TC centre, and V_{max}.

The inputs parameters required to construct both the wind and surface pressure fields, namely the TC centre position, the azimuthally averaged maximum wind speed V_{max}, and the wind radii, are obtained from the IBTrACS dataset. IBTrACS parameters (see Section 2.1, hereafter denoted with IBT) are not representative of azimuthally averaged parameters (Avenas et al., 2023) as $V_{max,IBT}$ being the local maximum of the 2D wind field, and $R_{34,IBT}$, $R_{50,IBT}$ and $R_{64,IBT}$ radii representing the maximum quadrant-averaged radial extent at which the respective wind thresholds are reached. Therefore, the following corrections (Herry et al., 2025) are applied to convert the IBTrACS values into an azimuthally averaged representation suitable for a TC parametric wind model:

$$\begin{cases} V_{max} = \frac{V_{max,IBT}}{1.186} \\ R_{64} = \frac{R_{64,IBT}}{1.044} \\ R_{50} = \frac{R_{50,IBT}}{1.238} \\ R_{34} = \frac{R_{34,IBT}}{1.342} \end{cases} \tag{A.10}$$

A.3. Bulk algorithms of wind stress

The wind stress τ represents the turbulent flux of momentum across the air–sea interface. In the simulations, because turbulent fluctuations cannot be explicitly represented, this flux is parametrised using classical bulk formulations, which links this surface turbulent flux to mean atmospheric quantities, through an exchange coefficient, the drag coefficient C_d, such as:

$$\tau = -\rho_a\overline{u'w'} = \rho_a u_*^2 = \rho_a C_d U_{10}^2 \tag{A.11}$$

where ρ_a is the air density, u' and w' the turbulent fluctuations of the horizontal and vertical wind components, respectively, u^* the friction velocity, and U_{10} the wind speed at 10 m above the surface. A term u_g is included in the computation of the wind module to take into account gust effects, Eq. (A.11) is then modified as follows (Fairall et al., 2003):

$$\tau = \rho_a C_d U_{10} U'_{10} \text{ where } U'_{10} = \sqrt{U_{10}^2 + u_g^2}. \tag{A.12}$$

The friction velocity is linked to the roughness length z_0, such as:

$$z_0 = \frac{\alpha u_*^2}{g} + \frac{0.11\nu}{u_*} \tag{A.13}$$

where g is the gravitational acceleration, ν the kinematic viscosity of air, and α the Charnock parameter.

Most simulations uses the COARE 3.0 bulk formulation (Fairall et al., 2003). In this parametrisation, the Charnock parameter is set to 0.011 for wind speeds up to 10 m.s^{-1}, increases linearly to 0.018 between 10 and 18 m.s^{-1}, and is kept constant beyond. Alternatively, the ECUMEv6 bulk formulation (Roehrig et al., 2020) is used, in which the surface exchange coefficients are directly derived from observations without explicitly parametrising the roughness length. Fig. A.16 shows the evolution of the mean drag coefficient C_D with respect to 10-m winds, averaged in 2 m.s^{-1} bins, from simulations using either COARE 3.0 (REF) or ECUMEv6 (τECM).

Data availability

All data used in this study are available online or can be obtained from the corresponding author upon request. Saint Martin tide gauge data and 0.001° bathymetry product are available on the SHOM platform (https://data.shom.fr). Tide gauge data for Barbuda can be retrieved from Unesco Sea Level Station Monitoring Facility (https://www.ioc-sealevelmonitoring.org/station.php?code=barb). The IBTrACS v4.01 dataset is available from NOAA's National Centers for Environmental Information (https://www.ncei.noaa.gov/products/international-best-track-archive). The SAR image of hurricane Irma is provided by CyclObs (https://cyclobs.ifremer.fr/app/tropical). The toolbox used to generate blended TC wind fields is available at https://doi.org/10.12770/11057ae4-b708-481a-9848-2e4fdef57625. ERA5 global reanalysis data are downloadable on the Climate Data Store (https://cds.climate.copernicus.eu/datasets/reanalysis-era5-single-levels?tab=overview). CMEMS data, used for initial and boundary conditions of simulations are available from the Copernicus Marine Data Store (https://data.marine.copernicus.eu/product/GLOBAL_MULTIYEAR_PHY_001_030/description). CROCO ocean model can be downloaded at https://doi.org/10.5281/zenodo.15064113. Analyses and figures were conducted with Python scripts, using Helmus and Collis (2016) Python package for colour-blind friendly colourmaps. The scripts are available from the corresponding author upon request.

References

Agulles, M., Marcos, M., Amores, A., Toomey, T., 2024. Storm surge modelling along European coastlines: The effect of the spatio-temporal resolution of the atmospheric forcing. Ocean. Model. 192, 102432. http://dx.doi.org/10.1016/j.ocemod.2024.102432, URL: https://www.sciencedirect.com/science/article/pii/S1463500324001197.

Arpaia, L., Ricchiuto, M., Filippini, A.G., Pedreros, R., 2021. An efficient 3d/2d-covariant formulation of the spherical shallow water equations: well balanced DG approximation and application to tsunami and storm surge. URL: https://brgm.hal.science/hal-03207171.

Avenas, A., Mouche, A., Tandeo, P., Piolle, J.F., Chavas, D., Fablet, R., Knaff, J., Chapron, B., 2023. Reexamining the estimation of tropical cyclone radius of maximum wind from outer size with an extensive synthetic aperture radar dataset. Mon. Weather Rev. 151 (12), 3169–3189. http://dx.doi.org/10.1175/MWR-D-23-0119.1, URL: https://journals.ametsoc.org/view/journals/mwre/151/12/MWR-D-23-0119.1.xml, Publisher: American Meteorological Society Section: Monthly Weather Review.

Barbary, D., Leroux, M.-D., Bousquet, O., 2019. The orographic effect of Reunion Island on tropical cyclone track and intensity. Atmospheric Sci. Lett. 20 (2), e882. http://dx.doi.org/10.1002/asl.882, URL: https://onlinelibrary.wiley.com/doi/abs/10.1002/asl.882, _eprint: https://onlinelibrary.wiley.com/doi/pdf/10.1002/asl.882.

Bertin, X., Li, K., Roland, A., Bidlot, J.-R., 2015. The contribution of short-waves in storm surges: Two case studies in the Bay of Biscay. Cont. Shelf Res. 96, 1–15. http://dx.doi.org/10.1016/j.csr.2015.01.005, URL: https://www.sciencedirect.com/science/article/pii/S0278434315000151.

Bian, G.F., Nie, G.Z., Qiu, X., 2021. How well is outer tropical cyclone size represented in the ERA5 reanalysis dataset? Atmos. Res. 249, 105339. http://dx.doi.org/10.1016/j.atmosres.2020.105339.

Boose, E.R., Serrano, M.I., Foster, D.R., 2004. Landscape and regional impacts of Hurricanes in puerto rico. Ecol. Monograph. 74 (2), 335–352. http://dx.doi.org/10.1890/02-4057, URL: https://onlinelibrary.wiley.com/doi/abs/10.1890/02-4057.

Bouwer, L.M., Jonkman, S.N., 2018. Global mortality from storm surges is decreasing. Environ. Res. Lett. 13 (1), 014008. http://dx.doi.org/10.1088/1748-9326/aa98a3, Publisher: IOP Publishing.

Bryant, K.M., Akbar, M., Bryant, K.M., Akbar, M., 2016. An exploration of wind stress calculation techniques in Hurricane storm surge modeling. J. Mar. Sci. Eng. 4 (3), http://dx.doi.org/10.3390/jmse4030058, URL: https://www.mdpi.com/2077-1312/4/3/58, Company: Multidisciplinary Digital Publishing Institute Distributor: Multidisciplinary Digital Publishing Institute Institution: Multidisciplinary Digital Publishing Institute Label: Multidisciplinary Digital Publishing Institute Publisher: publisher.

Cangialosi, J.P., S. Latto, A., Berg, R., 2021. Hurricane Irma. Tropical Cyclone Report, National Hurricane Center, URL: https://www.nhc.noaa.gov/data/tcr/AL112017_Irma.pdf.

Cécé, R., Bernard, D., Krien, Y., Leone, F., Candela, T., Péroche, M., Biabiany, E., Arnaud, G., Belmadani, A., Palany, P., Zahibo, N., 2021. A 30 m scale modeling of extreme gusts during Hurricane Irma (2017) landfall on very small mountainous islands in the Lesser Antilles. Nat. Hazards Earth Syst. Sci. 21 (1), 129–145. http://dx.doi.org/10.5194/nhess-21-129-2021, URL: https://nhess.copernicus.org/articles/21/129/2021/, Publisher: Copernicus GmbH.

Chaigneau, A.A., Menéndez, M., Ramírez-Pérez, M., Toimil, A., 2024. Regional modelling of extreme sea levels induced by Hurricanes. Nat. Hazards Earth Syst. Sci. 24 (11), 4109–4131. http://dx.doi.org/10.5194/nhess-24-4109-2024, URL: https://nhess.copernicus.org/articles/24/4109/2024/, Publisher: Copernicus GmbH.

Chambers, C.R.S., Li, T., 2011. The effect of Hawai'i's big island on track and structure of tropical cyclones passing to the south and west. Mon. Weather Rev. 139 (11), 3609–3627. http://dx.doi.org/10.1175/MWR-D-11-00031.1, URL: https://journals.ametsoc.org/view/journals/mwre/139/11/mwr-d-11-00031.1.xml, Publisher: American Meteorological Society Section: Monthly Weather Review.

Chavas, D.R., Knaff, J.A., 2022. A simple model for predicting the tropical cyclone radius of maximum wind from outer size. Weather Forecast. 37 (5), 563–579. http://dx.doi.org/10.1175/WAF-D-21-0103.1, URL: https://journals.ametsoc.org/view/journals/wefo/37/5/WAF-D-21-0103.1.xml.

Chen, J., Chavas, D.R., 2020. The transient responses of an axisymmetric tropical cyclone to instantaneous surface roughening and drying. J. Atmos. Sci. 77 (8), 2807–2834. http://dx.doi.org/10.1175/JAS-D-19-0320.1, URL: https://journals.ametsoc.org/view/journals/atsc/77/8/jasD190320.xml.

Combot, C., Mouche, A., Knaff, J., Zhao, Y., Zhao, Y., Vinour, L., Quilfen, Y., Chapron, B., 2020. Extensive high-resolution synthetic aperture radar (SAR) data analysis of tropical cyclones: Comparisons with SFMR flights and best track. Mon. Weather Rev. 148 (11), 4545–4563. http://dx.doi.org/10.1175/MWR-D-20-0005.1, URL: https://journals.ametsoc.org/view/journals/mwre/148/11/MWR-D-20-0005.1.xml, Publisher: American Meteorological Society Section: Monthly Weather Review.

Debreu, L., Marchesiello, P., Penven, P., Cambon, G., 2012. Two-way nesting in split-explicit ocean models: Algorithms, implementation and validation. Ocean. Model. 49–50, 1–21. http://dx.doi.org/10.1016/j.ocemod.2012.03.003, URL: https://www.sciencedirect.com/science/article/pii/S1463500312000480.

DeMaria, M., Franklin, J.L., Onderlinde, M.J., Kaplan, J., DeMaria, M., Franklin, J.L., Onderlinde, M.J., Kaplan, J., 2021. Operational forecasting of tropical cyclone rapid intensification at the national Hurricane center. Atmosphere 12 (6), http://dx.doi.org/10.3390/atmos12060683, URL: https://www.mdpi.com/2073-4433/12/6/683, Company, Distributor, Institution, Label: Multidisciplinary Digital Publishing Institute.

DeMaria, M., Knaff, J.A., Kaplan, J., 2006. On the decay of tropical cyclone winds crossing narrow landmasses. J. Appl. Meteorol. Clim. 45 (3), 491–499. http://dx.doi.org/10.1175/JAM2351.1, URL: https://journals.ametsoc.org/view/journals/apme/45/3/jam2351.1.xml, Publisher: American Meteorological Society Section: Journal of Applied Meteorology and Climatology.

Dulac, W., Cattiaux, J., Chauvin, F., Bourdin, S., Fromang, S., 2024. Assessing the representation of tropical cyclones in ERA5 with the CNRM tracker. Clim. Dyn. 62 (1), 223–238. http://dx.doi.org/10.1007/s00382-023-06902-8.

Dullaart, J.C.M., Muis, S., Bloemendaal, N., Aerts, J.C.J.H., 2020. Advancing global storm surge modelling using the new ERA5 climate reanalysis. Clim. Dyn. 54 (1), 1007–1021. http://dx.doi.org/10.1007/s00382-019-05044-0, URL: https://doi.org/10.1007/s00382-019-05044-0.

Echevarria, E., Hoeke, R., Trenham, C., Ramsay, H., Hernaman, V., McInnes, K., O'Grady, J., Contardo, S., Khan, S., Meucci, A., 2026. Evaluation of parametric tropical cyclone wind models for representing storm surge and wave heights in the queensland region. Ocean. Model. 202, 102737. http://dx.doi.org/10.1016/j.ocemod.2026.102737, URL: https://www.sciencedirect.com/science/article/pii/S1463500326000612.

Egbert, G.D., Erofeeva, S.Y., 2002. Efficient inverse modeling of barotropic ocean tides. J. Atmos. Ocean. Technol. 19 (2), 183–204. http://dx.doi.org/10.1175/1520-0426(2002)019<0183:EIMOBO>2.0.CO;2, URL: https://journals.ametsoc.org/view/journals/atot/19/2/1520-0426_2002_019_0183_eimobo_2_0_co_2.xml, Publisher: American Meteorological Society Section: Journal of Atmospheric and Oceanic Technology.

Emanuel, K., 2018. 100 Years of progress in tropical cyclone research. Meteorol. Monogr. 59 (1), 15.1–15.68. http://dx.doi.org/10.1175/AMSMONOGRAPHS-D-18-0016.1, URL: https://journals.ametsoc.org/view/journals/amsm/59/1/amsmonographs-d-18-0016.1.xml, Publisher: American Meteorological Society Section: Meteorological Monographs.

Fairall, C.W., Bradley, E.F., Hare, J.E., Grachev, A.A., Edson, J.B., 2003. Bulk parameterization of air–sea fluxes: Updates and verification for the COARE algorithm. J. Clim. 16 (4), 571–591. http://dx.doi.org/10.1175/1520-0442(2003)016<0571:BPOASF>2.0.CO;2, URL: https://journals.ametsoc.org/view/journals/clim/16/4/1520-0442_2003_016_0571_bpoasf_2.0.co_2.xml, Publisher: American Meteorological Society Section: Journal of Climate.

Gahtan, J., Knapp, K., Schreck, C., Diamond, H.J., Kossin, J.P., Kruk, M.C., 2024. International best track archive for climate stewardship (IBTrACS) project, version 4r01. NOAA Natl. Centers Environ. Inf. 10, http://dx.doi.org/10.25921/82ty-9e16.

Glavovic, B., Dawson, R., CHOW, W.T., Garschagen, M., Singh, C., Thomas, A., 2022. Cross-chapter paper 2: Cities and settlements by the sea. In: Pörtner, H.O., Roberts, D.C., Tignor, M., Poloczanska, E.S., Mintenbeck, K., Alegrí a, A., Craig, M., Langsdorf, S., Löschke, S., Möller, V., Okem, A., Rama, B. (Eds.), Climate Change 2022: Impacts, Adaptation and Vulnerability. Contribution of Working Group

II To the Sixth Assessment Report of the Intergovernmental Panel on Climate Change. Cambridge University Press, Cambridge, UK and New York, NY, USA, pp. 2163–2194. http://dx.doi.org/10.1017/9781009325844.019.

Haasnoot, M., Winter, G., Brown, S., Dawson, R.J., Ward, P.J., Eilander, D., 2021. Long-term sea-level rise necessitates a commitment to adaptation: A first order assessment. Clim. Risk Manag. 34, 100355. http://dx.doi.org/10.1016/j.crm.2021.100355, URL: https://www.sciencedirect.com/science/article/pii/S221209632100084X.

Helmus, J.J., Collis, S.M., 2016. The python ARM radar toolkit (Py-ART), a library for working with weather radar data in the python programming language. J. Open Res. Softw. 4, http://dx.doi.org/10.5334/jors.119, URL: https://openresearchsoftware.metajnl.com/articles/jors.119.

Herry, N., Jullien, S., Vinour, L., Zribi, A., Menkes, C., 2025. A new reconstruction method for generating a realistic tropical cyclone wind field. Mon. Weather Rev. URL: https://hal.science/hal-05427687, Preprint.

Hersbach, H., Bell, B., Berrisford, P., Hirahara, S., Horányi, A., Muñoz-Sabater, J., Nicolas, J., Peubey, C., Radu, R., Schepers, D., Simmons, A., Soci, C., Abdalla, S., Abellan, X., Balsamo, G., Bechtold, P., Biavati, G., Bidlot, J., Bonavita, M., De Chiara, G., Dahlgren, P., Dee, D., Diamantakis, M., Dragani, R., Flemming, J., Forbes, R., Fuentes, M., Geer, A., Haimberger, L., Healy, S., Hogan, R.J., Hólm, E., Janisková, M., Keeley, S., Laloyaux, P., Lopez, P., Lupu, C., Radnoti, G., de Rosnay, P., Rozum, I., Vamborg, F., Villaume, S., Thépaut, J.N., 2020. The ERA5 global reanalysis. Q. J. R. Meteorol. Soc. 146 (730), 1999–2049. http://dx.doi.org/10.1002/qj.3803, URL: https://onlinelibrary.wiley.com/doi/abs/10.1002/qj.3803, _eprint: https://rmets.onlinelibrary.wiley.com/doi/pdf/10.1002/qj.3803.

Hodges, K., Cobb, A., Vidale, P.L., 2017. How well are tropical cyclones represented in reanalysis datasets? J. Clim. 30 (14), 5243–5264. http://dx.doi.org/10.1175/JCLI-D-16-0557.1, URL: https://journals.ametsoc.org/view/journals/clim/30/14/jcli-d-16-0557.1.xml, Publisher: American Meteorological Society Section: Journal of Climate.

Holthuijsen, L.H., Powell, M.D., Pietrzak, J.D., 2012. Wind and waves in extreme Hurricanes. J. Geophys. Res.: Ocean. 117 (C9), http://dx.doi.org/10.1029/2012JC007983, URL: https://onlinelibrary.wiley.com/doi/abs/10.1029/2012JC007983.

Irish, J.L., Resio, D.T., Ratcliff, J.J., 2008. The influence of storm size on Hurricane surge. J. Phys. Oceanogr. 38 (9), 2003–2013. http://dx.doi.org/10.1175/2008JPO3727.1, URL: https://journals.ametsoc.org/view/journals/phoc/38/9/2008jpo3727.1.xml, Publisher: American Meteorological Society Section: Journal of Physical Oceanography.

Jullien, S., Aucan, J., Kestenare, E., Lengaigne, M., Menkes, C., 2024. Unveiling the global influence of tropical cyclones on extreme waves approaching coastal areas. Nat. Commun. 15 (1), 6593. http://dx.doi.org/10.1038/s41467-024-50929-2, URL: https://www.nature.com/articles/s41467-024-50929-2, Publisher: Nature Publishing Group.

Kang, H., Du, S., Wu, G., Liang, B., Shi, L., Wang, X., Yang, B., Wang, Z., 2026. Quantifying the uncertainties in projecting Extreme Coastal hazards: The overlooked role of the radius of maximum wind parameterizations. J. Mar. Sci. Eng. 14 (2), http://dx.doi.org/10.3390/jmse14020222, URL: https://www.mdpi.com/2077-1312/14/2/222.

Kaplan, J., DeMaria, M., 1995. A simple empirical model for predicting the decay of tropical cyclone winds after landfall. J. Appl. Meteorol. Clim. 34 (11), 2499–2512. http://dx.doi.org/10.1175/1520-0450(1995)034<2499:ASEMFP>2.0.CO;2, URL: https://journals.ametsoc.org/view/journals/apme/34/11/1520-0450_1995_034_2499_asemfp_2_0_co_2.xml, Publisher: American Meteorological Society Section: Journal of Applied Meteorology and Climatology.

Kennedy, A.B., Westerink, J.J., Smith, J.M., Hope, M.E., Hartman, M., Taflanidis, A.A., Tanaka, S., Westerink, H., Cheung, K.F., Smith, T., Hamann, M., Minamide, M., Ota, A., Dawson, C., 2012. Tropical cyclone inundation potential on the hawaiian islands of oahu and kauai. Ocean. Model. 52–53, 54–68. http://dx.doi.org/10.1016/j.ocemod.2012.04.009, URL: https://www.sciencedirect.com/science/article/pii/S1463500312000698.

Knaff, J.A., Zehr, R.M., 2007. Reexamination of tropical cyclone wind–pressure relationships. Weather. Forecast. 22 (1), 71–88. http://dx.doi.org/10.1175/WAF965.1, URL: https://journals.ametsoc.org/view/journals/wefo/22/1/waf965_1.xml, Publisher: American Meteorological Society Section: Weather and Forecasting.

Knapp, K.R., Kruk, M.C., Levinson, D.H., Diamond, H.J., Neumann, C.J., 2010. The international best track archive for climate stewardship (IBTrACS): Unifying tropical cyclone data. Bull. Am. Meteorol. Soc. 91 (3), 363–376. http://dx.doi.org/10.1175/2009BAMS2755.1, URL: https://journals.ametsoc.org/view/journals/bams/91/3/2009bams2755_1.xml, Publisher: American Meteorological Society Section: Bulletin of the American Meteorological Society.

Landsea, C.W., Franklin, J.L., 2013. Atlantic Hurricane database uncertainty and presentation of a new database format. Mon. Weather Rev. 141 (10), 3576–3592. http://dx.doi.org/10.1175/MWR-D-12-00254.1, URL: https://journals.ametsoc.org/view/journals/mwre/141/10/mwr-d-12-00254.1.xml, Publisher: American Meteorological Society Section: Monthly Weather Review.

Large, W.G., McWilliams, J.C., Doney, S.C., 1994. Oceanic vertical mixing: A review and a model with a nonlocal boundary layer parameterization. Rev. Geophys. 32 (4), 363–403. http://dx.doi.org/10.1029/94RG01872, URL: https://onlinelibrary.wiley.com/doi/abs/10.1029/94RG01872.

Lavaud, L., Bertin, X., Martins, K., Arnaud, G., Bouin, M.N., 2020. The contribution of short-wave breaking to storm surges: The case klaus in the southern bay of biscay. Ocean. Model. 156, 101710. http://dx.doi.org/10.1016/j.ocemod.2020.101710, URL: https://www.sciencedirect.com/science/article/pii/S1463500320302122.

Lemarié, F., Debreu, L., Shchepetkin, A.F., McWilliams, J.C., 2012. On the stability and accuracy of the harmonic and biharmonic isoneutral mixing operators in ocean models. Ocean. Model. 52–53, 9–35. http://dx.doi.org/10.1016/j.ocemod.2012.04.007, URL: https://www.sciencedirect.com/science/article/pii/S1463500312000674.

Marchesiello, P., Debreu, L., Couvelard, X., 2009. Spurious diapycnal mixing in terrain-following coordinate models: The problem and a solution. Ocean. Model. 26 (3), 156–169. http://dx.doi.org/10.1016/j.ocemod.2008.09.004, URL: https://www.sciencedirect.com/science/article/pii/S1463500308001510.

Marchesiello, P., McWilliams, J.C., Shchepetkin, A., 2001. Open boundary conditions for long-term integration of regional oceanic models. Ocean. Model. 3 (1), 1–20. http://dx.doi.org/10.1016/S1463-5003(00)00013-5, URL: https://www.sciencedirect.com/science/article/pii/S1463500300000135.

Martin Miguez, B., Testut, L., Wöppelmann, G., 2012. Performance of modern tide gauges: towards mm-level accuracy. Sci. Mar. 76 (S1), 221–228, URL: https://hal.science/hal-00799020v1.

Mastenbroek, C., Burgers, G., Janssen, P.A.E.M., 1993. The dynamical coupling of a wave model and a storm surge model through the atmospheric boundary layer. J. Phys. Oceanogr. 23 (8), 1856–1866. http://dx.doi.org/10.1175/1520-0485(1993)023<1856:TDCOAW>2.0.CO;2, URL: https://journals.ametsoc.org/view/journals/phoc/23/8/1520-0485_1993_023_1856_tdcoaw_2_0_co_2.xml.

Moon, I.J., Kwon, J.I., Lee, J.C., Shim, J.S., Kang, S.K., Oh, I.S., Kwon, S.J., 2009. Effect of the surface wind stress parameterization on the storm surge modeling. Ocean. Model. 29 (2), 115–127. http://dx.doi.org/10.1016/j.ocemod.2009.03.006, URL: https://www.sciencedirect.com/science/article/pii/S146350030900064X.

Mouche, A., Chapron, B., Knaff, J., Zhao, Y., Zhang, B., Combot, C., 2019. Copolarized and cross-polarized SAR measurements for high-resolution description of major Hurricane wind structures: Application to Irma category 5 Hurricane. J. Geophys. Res.: Ocean. 124 (6), 3905–3922. http://dx.doi.org/10.1029/2019JC015056, URL: https://onlinelibrary.wiley.com/doi/abs/10.1029/2019JC015056.

Mouche, A.A., Chapron, B., Zhang, B., Husson, R., 2017. Combined co- and cross-polarized SAR measurements under extreme wind conditions. IEEE Trans. Geosci. Remote Sens. 55 (12), 6746–6755. http://dx.doi.org/10.1109/TGRS.2017.2732508, URL: https://ieeexplore.ieee.org/document/8016397.

Muis, S., Verlaan, M., Winsemius, H.C., Aerts, J.C.J.H., Ward, P.J., 2016. A global reanalysis of storm surges and extreme sea levels. Nat. Commun. 7 (1), 11969. http://dx.doi.org/10.1038/ncomms11969, URL: https://www.nature.com/articles/ncomms11969, Publisher: Nature Publishing Group.

Needham, H.F., Keim, B.D., Sathiaraj, D., 2015. A review of tropical cyclone-generated storm surges: Global data sources, observations, and impacts. Rev. Geophys. 53 (2), 545–591. http://dx.doi.org/10.1002/2014RG000477, URL: https://onlinelibrary.wiley.com/doi/abs/10.1002/2014RG000477.

Neumann, B., Vafeidis, A.T., Zimmermann, J., Nicholls, R.J., 2015. Future coastal population growth and exposure to sea-level rise and coastal flooding - A global assessment. PLoS One 10 (3), e0118571. http://dx.doi.org/10.1371/journal.pone.0118571, URL: https://journals.plos.org/plosone/article?id=10.1371/journal.pone.0118571, Publisher: Public Library of Science.

Nicholls, R.J., 2006. Storm surges in coastal areas. In: Natural Disaster Hotspots, Case Studies. In: The World Bank Hazard Management Unit, Disaster Risk Management Series, vol. 6, pp. 79–108.

Nicolle, A., Karpytchev, M., Benoit, M., 2009. Amplification of the storm surges in shallow waters of the Pertuis Charentais (Bay of Biscay, France). Ocean. Dyn. 59 (6), 921–935. http://dx.doi.org/10.1007/s10236-009-0219-0.

OCHA, 2008. Myanmar Cyclone Nargis. Situation Report 39, Office for the coordination of humanitarian affairs, United Nations, URL: https://www.unocha.org/publications/report/myanmar/myanmar-cyclone-nargis-ocha-situation-report-no-39.

O'Grady, J., Ramsay, H., McInnes, K., Gregory, R., 2024. Evaluation of parametric tropical cyclone surface winds over the eastern Australian region. Mon. Weather. Rev. 152 (1), 345–361. http://dx.doi.org/10.1175/MWR-D-23-0063.1, URL: https://journals.ametsoc.org/view/journals/mwre/152/1/MWR-D-23-0063.1.xml.

Olfateh, M., Callaghan, D.P., Nielsen, P., Baldock, T.E., 2017. Tropical cyclone wind field asymmetry—Development and evaluation of a new parametric model. J. Geophys. Res.: Ocean. 122 (1), 458–469. http://dx.doi.org/10.1002/2016JC012237, URL: https://onlinelibrary.wiley.com/doi/abs/10.1002/2016JC012237.

Oppenheimer, M., Glavovic, B., Hinkel, J., Van de Wal, R., Magnan, A.K., Abd-Elgawad, A., Cai, R., Cifuentes-Jara, M., Deconto, R.M., Ghosh, T., Hay, J., Isla, F., Marzeion, B., Z, S., 2019. Sea level rise and implications for low lying islands, coasts and communities. In: Pörtner, H., D.C., R., Masson-Delmote, V., Zhai, P., Tignor, M., Poloczanska, E., Mintenbeck, K., Alegría, A., Nicolai, M., Oken, A., Petzold, J., Rama, B., Weyer, N. (Eds.), IPCC Special Report on the Ocean and Cryosphere in a Changing Climate. The Intergovernmental Panel on Climate Change, pp. 321–445. http://dx.doi.org/10.1017/9781009157964.006.

Paugam, C., Sous, D., Rey, V., Meulé, S., Faure, V., Boutron, O., Luna-Laurent, E., Migne, E., 2021. Wind tides and surface friction coefficient in semi-enclosed shallow lagoons. Estuar. Coast. Shelf Sci. 257, 107406. http://dx.doi.org/10.1016/j.ecss.2021.107406, URL: https://www.sciencedirect.com/science/article/pii/S0272771421002596.

Peng, M., Xie, L., Pietrafesa, L.J., 2006. Tropical cyclone induced asymmetry of sea level surge and fall and its presentation in a storm surge model with parametric wind fields. Ocean. Model. 14 (1), 81–101. http://dx.doi.org/10.1016/j.ocemod.2006.03.004, URL: https://www.sciencedirect.com/science/article/pii/S1463500306000291.

Pineau-Guillou, L., 2018. Ocean-Atmosphere Interaction : Improvement of Wind Stress for Coastal Physical Modelling (Ph.D. thesis). Université de Bretagne occidentale - Brest, URL: https://theses.hal.science/tel-02076492.

Pineau-Guillou, L., Bouin, M.-N., Ardhuin, F., Lyard, F., Bidlot, J.-R., Chapron, B., 2020. Impact of wave-dependent stress on storm surge simulations in the North Sea: Ocean model evaluation against in situ and satellite observations. Ocean. Model. 154, 101694. http://dx.doi.org/10.1016/j.ocemod.2020.101694, URL: https://www.sciencedirect.com/science/article/pii/S1463500320301967.

Powell, M.D., Vickery, P.J., Reinhold, T.A., 2003. Reduced drag coefficient for high wind speeds in tropical cyclones. Nature 422 (6929), 279–283. http://dx.doi.org/10.1038/nature01481.

Proudman, J., 1957. Oscillations of tide and surge in an estuary of finite length. J. Fluid Mech. 2 (4), 371–382. http://dx.doi.org/10.1017/S002211205700018X, URL: https://www.cambridge.org/core/journals/journal-of-fluid-mechanics/article/abs/oscillations-of-tide-and-surge-in-an-estuary-of-finite-length/E161FCFEB8741203E2247E8BB5DC25AE.

Pytharouli, S., Chaikalis, S., Stiros, S.C., 2018. Uncertainty and bias in electronic tide-gauge records: Evidence from collocated sensors. Measurement 125, 496–508. http://dx.doi.org/10.1016/j.measurement.2018.05.012, URL: https://www.sciencedirect.com/science/article/pii/S0263224118303968.

Ramos-Valle, A.N., Curchitser, E.N., Bruyère, C.L., 2020. Impact of tropical cyclone landfall angle on storm surge along the mid-atlantic bight. J. Geophys. Res.: Atmospheres 125 (4), http://dx.doi.org/10.1029/2019JD031796, e2019JD031796, URL: https://onlinelibrary.wiley.com/doi/abs/10.1029/2019JD031796.

Rego, J.L., Li, C., 2009. On the importance of the forward speed of Hurricanes in storm surge forecasting: A numerical study. Geophys. Res. Lett. 36 (7), http://dx.doi.org/10.1029/2008GL036953, URL: https://onlinelibrary.wiley.com/doi/abs/10.1029/2008GL036953.

Rey, T., Leone, F., Candela, T., Belmadani, A., Palany, P., Krien, Y., Cécé, R., Gherardi, M., Péroche, M., Zahibo, N., 2019. Coastal processes and influence on damage to urban structures during Hurricane Irma (St-Martin & St-Barthélemy, French West Indies). J. Mar. Sci. Eng. 7 (7), 215. http://dx.doi.org/10.3390/jmse7070215, URL: https://www.mdpi.com/2077-1312/7/7/215, Publisher: Multidisciplinary Digital Publishing Institute.

Ridder, N., de Vries, H., Drijfhout, S., van den Brink, H., van Meijgaard, E., de Vries, H., 2018. Extreme storm surge modelling in the North Sea. Ocean. Dyn. 68 (2), 255–272. http://dx.doi.org/10.1007/s10236-018-1133-0.

Roehrig, R., Beau, I., Saint-Martin, D., Alias, A., Decharme, B., Guérémy, J.F., Voldoire, A., Abdel-Lathif, A.Y., Bazile, E., Belamari, S., Blein, S., Bouniol, D., Bouteloup, Y., Cattiaux, J., Chauvin, F., Chevallier, M., Colin, J., Douville, H., Marquet, P., Michou, M., Nabat, P., Oudar, T., Peyrillé, P., Piriou, J.-M., Salas y Mélia, D., Séférian, R., Sénési, S., 2020. The CNRM global atmosphere model ARPEGE-climat 6.3: Description and evaluation. J. Adv. Model. Earth Syst. 12 (7), http://dx.doi.org/10.1029/2020MS002075, e2020MS002075, URL: https://onlinelibrary.wiley.com/doi/abs/10.1029/2020MS002075.

Schenkel, B.A., Lin, N., Chavas, D., Oppenheimer, M., Brammer, A., 2017. Evaluating outer tropical cyclone size in reanalysis datasets using QuikSCAT data. J. Clim. 30 (21), 8745–8762. http://dx.doi.org/10.1175/JCLI-D-17-0122.1, URL: https://journals.ametsoc.org/view/journals/clim/30/21/jcli-d-17-0122.1.xml, Publisher: American Meteorological Society Section: Journal of Climate.

Schenkel, B.A., Noble, C., Chavas, D., Chan, K.T., Barlow, S.J., Singh, A., Musgrave, K., 2023. Recent progress in research and forecasting of tropical cyclone outer size. Trop. Cyclone Res. Rev. 12 (3), 151–164. http://dx.doi.org/10.1016/j.tcrr.2023.09.002, URL: https://www.sciencedirect.com/science/article/pii/S2225603223000401.

Sebastian, M., Behera, M.R., 2022. Impact of highest maximum sustained wind speed and its duration on storm surges and hydrodynamics along Krishna–Godavari coast. Clim. Dyn. 59 (3), 1057–1078. http://dx.doi.org/10.1007/s00382-022-06173-9.

Shchepetkin, A.F., McWilliams, J.C., 2003. A method for computing horizontal pressure-gradient force in an oceanic model with a nonaligned vertical coordinate. J. Geophys. Res.: Ocean. 108 (C3), http://dx.doi.org/10.1029/2001JC001047, URL: https://onlinelibrary.wiley.com/doi/abs/10.1029/2001JC001047.

SHOM, 2017. Regional 500m bathymetric digital elevation model of the Antilles-Guyane zone for hydrodynamic modeling (Homonim project).

So, S., Juarez, B., Valle-Levinson, A., Gillin, M.E., 2019. Storm surge from Hurricane Irma along the Florida Peninsula. Estuar. Coast. Shelf Sci. 229, 106402. http://dx.doi.org/10.1016/j.ecss.2019.106402, URL: https://www.sciencedirect.com/science/article/pii/S0272771419302914.

Takagaki, N., Komori, S., Suzuki, N., Iwano, K., Kuramoto, T., Shimada, S., Kurose, R., Takahashi, K., 2012. Strong correlation between the drag coefficient and the shape of the wind sea spectrum over a broad range of wind speeds. Geophys. Res. Lett. 39 (23), http://dx.doi.org/10.1029/2012GL053988, URL: https://onlinelibrary.wiley.com/doi/abs/10.1029/2012GL053988.

Thomas, A., Dietrich, J., Asher, T., Bell, M., Blanton, B., Copeland, J., Cox, A., Dawson, C., Fleming, J., Luettich, R., 2019. Influence of storm timing and forward speed on tides and storm surge during Hurricane Matthew. Ocean. Model. 137, 1–19. http://dx.doi.org/10.1016/j.ocemod.2019.03.004, URL: https://www.sciencedirect.com/science/article/pii/S1463500318302609.

Torgerson, W., Schwendike, J., Ross, A., Short, C.J., 2023. Intensity fluctuations in Hurricane Irma (2017) during a period of rapid intensification. Weather. Clim. Dyn. 4 (2), 331–359. http://dx.doi.org/10.5194/wcd-4-331-2023, URL: https://wcd.copernicus.org/articles/4/331/2023/, Publisher: Copernicus GmbH.

Torn, R.D., Snyder, C., 2012. Uncertainty of tropical cyclone best-track information. Weather. Forecast. 27 (3), 715–729. http://dx.doi.org/10.1175/WAF-D-11-00085.1, URL: https://journals.ametsoc.org/view/journals/wefo/27/3/waf-d-11-00085_1.xml, Publisher: American Meteorological Society Section: Weather and Forecasting.

Vinour, L., Jullien, S., Mouche, A., Avenas, A., 2025. Review and improvement of tropical cyclone surface wind parametric models using SAR imagery. J. Appl. Meteorol. Climatol. e240219. http://dx.doi.org/10.1175/JAMC-D-24-0219.1, URL: https://journals.ametsoc.org/view/journals/apme/aop/JAMC-D-24-0219.1/JAMC-D-24-0219.1.xml.

Weaver, R., Slinn, D., 2010. Influence of bathymetric fluctuations on coastal storm surge. Coast. Eng. 57 (1), 62–70. http://dx.doi.org/10.1016/j.coastaleng.2009.09.012, URL: https://www.sciencedirect.com/science/article/pii/S0378383909001513.

Weisberg, R.H., Zheng, L., 2006. Hurricane storm surge simulations for Tampa Bay. Estuaries Coasts 29 (6), 899–913. http://dx.doi.org/10.1007/BF02798649.

Willoughby, H.E., Darling, R.W.R., Rahn, M.E., 2006. Parametric representation of the primary Hurricane vortex. Part II: A new family of sectionally continuous profiles. Mon. Weather Rev. 134 (4), 1102–1120. http://dx.doi.org/10.1175/MWR3106.1, URL: http://journals.ametsoc.org/doi/10.1175/MWR3106.1.

Wood, V.T., White, L.W., Willoughby, H.E., Jorgensen, D.P., 2013. A new parametric tropical cyclone tangential wind profile model. Mon. Weather Rev. 141 (6), 1884–1909. http://dx.doi.org/10.1175/MWR-D-12-00115.1, URL: https://journals.ametsoc.org/view/journals/mwre/141/6/mwr-d-12-00115.1.xml.

Woodworth, P., Aarup, T., Gaël, A., Donato, V., Enet, S., Edwing, R., Heitsenrether, R., Farre, R., Fierro, J., Gaete, J., Foden, P., Pugh, J., Perez, B., Rickards, L., Schöne, T. (Eds.), 2016. Manual on sea-level measurements and interpretation, volume v: Radar gauges. In: IOC Manuals and Guides, vol. 14, (89), Intergovernmental Oceanographic Commission of UNESCO, Paris, URL: https://gfzpublic.gfz.de/pubman/faces/ViewItemFullPage.jsp?itemId=item_2041890_9, JCOMM Technical Report No. 89.

Wu, G., Shi, F., Kirby, J.T., Liang, B., Shi, J., 2018. Modeling wave effects on storm surge and coastal inundation. Coast. Eng. 140, 371–382. http://dx.doi.org/10.1016/j.coastaleng.2018.08.011, URL: https://www.sciencedirect.com/science/article/pii/S0378383918301388.

Wunsch, C., Stammer, D., 1997. Atmospheric loading and the oceanic "inverted barometer" effect. Rev. Geophys. 35 (1), 79–107. http://dx.doi.org/10.1029/96RG03037, URL: https://agupubs.onlinelibrary.wiley.com/doi/abs/10.1029/96RG03037.

Zhou, X., Hara, T., Ginis, I., D'Asaro, E., Hsu, J.-Y., Reichl, B.G., 2022. Drag coefficient and its sea state dependence under tropical cyclones. J. Phys. Oceanogr. 52 (7), 1447–1470. http://dx.doi.org/10.1175/JPO-D-21-0246.1, URL: https://journals.ametsoc.org/view/journals/phoc/52/7/JPO-D-21-0246.1.xml, Publisher: American Meteorological Society Section: Journal of Physical Oceanography.